Analytical assessment of Kelvin-Helmholtz instability growth at Ganymede's upstream magnetopause

Nawapat Kaweeyanun¹, Adam Masters¹, and Xianzhe Jia²

¹Imperial College London ²University of Michigan-Ann Arbor

November 26, 2022

Abstract

Ganymede is the only Solar System moon that generates a permanent magnetic field. Dynamics inside Ganymede's magnetosphere is likely driven by energy-transfer interactions on its upstream magnetopause. Previously in Kaweeyanun et al. (2020), we created a steady-state analytical model of Ganymede's magnetopause and predicted global-scale magnetic reconnection to occur frequently throughout the surface. Using the same model, this paper provides the first assessment of Kelvin-Helmholtz (K-H) instability growth on the magnetopause in isolation from reconnection effects. The linear K-H instability growth rate is calculated at Ganymede's equatorial magnetopause flank points under the magnetohydrodynamic with finite Larmor radius effect (MHD-FLR) theory, which accounts for inter-flank growth rate asymmetry due to large gyroradii of Jovian plasma ions. The calculation gives growth rates between γ [?] 0.01-48 /s with notable enhancement at the equatorial flank point closer to Jupiter. Then, the ideal MHD K-H instability onset condition is evaluated across the entire Ganymedean magnetopause. We find the conditions along both magnetopause flanks to be K-H favorable at all latitudes with growth rates similar to those at respective equatorial flank points. Using Mercury's magnetopause case as a comparison, we determined that nonlinear K-H vortices are viable at Ganymede based on the calculated growth rates, but the vortex growth will likely be suppressed once global reconnection is taken into account.

1	Analytical assessment of Kelvin-Helmholtz instability growth at Ganymede's upstream
2	magnetopause
3	*N. Kaweeyanun(1), A. Masters(1), X. Jia(2)
5	
6	(1) Department of Physics, Imperial College London
7	(2) The Climate and Space Sciences and Engineering Department, University of Michigan
8	
9	Corresponding author: N.Kaweeyanun
10	Corresponding author email: <u>nk2814@ic.ac.uk</u>
11	
12	Key Points
13	• We present the first assessment of Kelvin-Helmholtz (K-H) instability on
14	Ganymede's magnetopause without magnetic reconnection effects.
15	• Ganymede's magnetopause flanks are K-H unstable with faster growth rates on the
16	near-Jupiter flank due to the finite Larmor radius effects.
17	• K-H vortices should be viable based on the growth rates, but their prevalence is likely
18	suppressed once reconnection effects are considered.
19	
20	Abstract
21	Ganymede is the only Solar System moon that generates a permanent magnetic field.
22	Dynamics inside Ganymede's magnetosphere is likely driven by energy-transfer interactions
23	on its upstream magnetopause. Previously in Kaweeyanun et al. (2020), we created a steady-
24	state analytical model of Ganymede's magnetopause and predicted global-scale magnetic

25 reconnection to occur frequently throughout the surface. Using the same model, this paper 26 provides the first assessment of Kelvin-Helmholtz (K-H) instability growth on the 27 magnetopause in isolation from reconnection effects. The linear K-H instability growth rate is 28 calculated at Ganymede's equatorial magnetopause flank points under the 29 magnetohydrodynamic with finite Larmor radius effect (MHD-FLR) theory, which accounts 30 for inter-flank growth rate asymmetry due to large gyroradii of Jovian plasma ions. The calculation gives growth rates between $\gamma \approx 0.01 - 48$ s⁻¹, with notable enhancement at the 31 32 equatorial flank point closer to Jupiter. Then, the ideal MHD K-H instability onset condition 33 is evaluated across the entire Ganymedean magnetopause. We find the conditions along both magnetopause flanks to be K-H favorable at all latitudes with growth rates similar to those at 34 respective equatorial flank points. Using Mercury's magnetopause case as a comparison, we 35 36 determined that nonlinear K-H vortices are viable at Ganymede based on the calculated 37 growth rates, but the vortex growth will likely be suppressed once global reconnection is 38 taken into account.

39

40 Plain Language Summary

41 Jupiter's largest moon Ganymede produces its own magnetic field, which is submerged 42 without mixing inside Jupiter's much larger magnetic field. The two magnetic fields meet 43 along a boundary called the upstream magnetopause, where Jupiter's plasma (energized gas) 44 is forced to flow around Ganymede at considerable speeds. This leads to a type of turbulent 45 motions known as Kelvin-Helmholtz (K-H) instability, which can twist the magnetopause into tightly coiled vortices and inject Jovian plasmas into Ganymede's magnetic field. These 46 47 injections are thought to drive plasma convection and space weather events (e.g. auroras) 48 near Ganymede. Here we determine potential locations and rates at which K-H instability can 49 grow along an idealized Ganymedean magnetopause surface with no competing interactions (e.g. magnetic reconnection), using a model previously established in Kaweeyanun et al.
(2020). Our results suggest that K-H instability can grow anywhere along both of
Ganymede's magnetopause flanks, with slightly faster growth rates on the flank closest to
Jupiter. By comparing the growth rates to those on Mercury's magnetopause, where K-H
vortices have been abundantly observed, we conclude that K-H vortices should be viable on
Ganymede's magnetopause flanks. However, once magnetic reconnection effects are taken
into account, K-H vortex growth will likely be strongly suppressed.

57

58 Key Words

Ganymede, Kelvin-Helmholtz instability, analytical model, finite Larmor radius effect,
magnetohydrodynamic theory

61

62 **1. Introduction**

63 Between 1996-2000, the Galileo spacecraft performed six flybys of Ganymede, the largest 64 moon of Jupiter and the Solar System, during which evidence of a permanent magnetic field 65 was detected (Kivelson et al., 1996; Gurnett et al., 1996). Ganymede's equatorial surface 66 magnetic field is ~7 times stronger than the ambient Jovian magnetic field, allowing 67 Ganymede to maintain a small distinct magnetosphere inside Jupiter's much larger one 68 (Kivelson et al., 1998; Kivelson et al., 2002). The primary source of Ganymede's magnetic 69 field is thought to be dynamo action inside an Earth-like molten iron core (Anderson et al., 70 1996; Schubert et al., 1996). The magnetic field is close to dipolar with a $\sim 176^{\circ}$ tilt between 71 the magnetic and rotation axes, but the angle varies by a few degrees between Galileo flybys 72 (Kivelson et al., 2002). The dipole tilt variation may be explained by non-negligible higher 73 order (e.g. quadrupole) moments in Ganymede's permanent magnetic field, or more likely a 74 large subsurface ocean whose convection generates a secondary induced magnetic field (Kivelson et al., 2002). This potential water presence makes Ganymede a primary destination
for the upcoming JUpiter ICy moon Explorer (JUICE) space mission (Grasset et al., 2013).

77

78 The Jovian magnetosphere around Ganymede is significantly populated by plasma released 79 from Io's volcanoes. The plasma diffuses outward over time, while rotating in the same 80 direction as Jupiter's rotation, to form a $\sim 3 R_I (R_I = 71,492 \text{ km})$ thick plasma sheet centered 81 around the Jovian centrifugal equator (Kivelson et al., 2004). This plane is tilted $\sim 7^{\circ}$ with 82 respect to Ganymede's orbit, which lies close to Jupiter's geographical equator plane, so the 83 moon experiences large variations in plasma and magnetic conditions as it moves up and 84 down through the plasma sheet (Kivelson et al., 2004). At Ganymede's average orbital 85 distance of 15 R_J, the Jovian plasma consists primarily of heavy oxygen and sulfur ions with 86 only 10% contribution from protons – a sharp contrast from the proton-dominated solar wind 87 (Bagenal et al., 2016). Furthermore, the Jovian plasma flow speed near Ganymede is sub-88 Alfvénic (i.e. magnetic pressure dominant) which leads to a cylindrical magnetosphere 89 (Neubauer, 1998), unlike the super-Alfvénic (i.e. dynamic pressure dominant) solar wind that 90 create bullet-shaped planetary magnetospheres (Neubauer, 1990). The environment around 91 Ganymede hence provides a unique laboratory to study plasma and magnetic interactions in 92 the Solar System.

93

Based on the magnetic topology, Ganymede's magnetosphere can be divided into "openfield" and "closed-field" regions. The open-field region includes most of Ganymede's polar caps. In this region, each magnetic field line connects from one of Ganymede's magnetic poles to the corresponding Jupiter's magnetic poles, forming an extended magnetotail structure known as the Alfvén wings (Neubauer, 1998; Jia, Kivelson et al., 2010). Under magnetohydrodynamic (MHD) theory, plasma particles can enter and escape Ganymede's 100 magnetosphere along these open field lines, but they do not have sufficiently large number or 101 velocity to influence dynamics inside the magnetosphere (Frank et al., 1997; Williams, 102 Mauk, & McEntire, 1997; Williams, Mauk, McEntire, Roelof et al., 1997). Meanwhile, the 103 closed-field region spans low-latitude areas upstream and downstream of Ganymede, in 104 which each magnetic field line has both ends at Ganymede's magnetic poles. On the 105 upstream side, the outermost closed magnetic field lines are compressed by ambient Jovian 106 magnetic field lines along a boundary known as the upstream magnetopause. Dynamics 107 inside Ganymede's magnetosphere are likely driven by interactions on the upstream 108 magnetopause, similar to a Dungey cycle in planetary magnetospheres (e.g. Jia, Walker et al., 109 2010; Collinson et al., 2018). Two of the most commonly studied magnetopause interactions 110 are magnetic reconnection and Kelvin-Helmholtz (K-H) instability. We have previously 111 investigated global magnetic reconnection at Ganymede's upstream magnetopause in 112 Kaweeyanun et al. (2020), therefore this paper will focus on the role of K-H instability in 113 energy transport into Ganymede's magnetosphere.

114

115 K-H instability arises from bulk flow shear between plasmas just outside and inside a magnetopause boundary. The instability can be divided into two distinct phases - a linear 116 117 phase in which the magnetopause develops wavelike oscillations (e.g. Dungey, 1955; 118 Southwood, 1968), followed by a nonlinear phase in which the waves grow into turbulent 119 vortices (e.g. Southwood, 1979; Miura, 1982). The nonlinear phase is particularly important 120 as multiple plasma/magnetic layers become tightly wound inside a K-H vortex, separated by very thin and unstable current sheets. These conditions can facilitate cross-magnetopause 121 122 energy transport via turbulent decay (Nakamura et al., 2004; Matsumoto & Hoshino, 2006), 123 coupling with kinetic Alfvén waves (Chaston et al., 2007), or inducing local magnetic 124 reconnection (Nykyri & Otto, 2001; Nakamura et al., 2006, 2008). The existence of linear K-

H waves at Ganymede's upstream magnetopause has been speculated from Galileo observations (Kivelson et al., 1998; Volwerk et al., 1999; Volwerk et al., 2013) and a numerical model (Tóth et al., 2016). However, there has not been a focused study on K-H vortices, or general K-H instability growth, at Ganymede's magnetopause.

129

130 The assessment detailed in this paper thus relies on K-H instability knowledge gained from 131 previous planetary magnetopause studies. Both K-H waves and vortices have been observed 132 at Earth's magnetopause, with evidence of energy transport in the vortex phase (Fairfield et 133 al., 2000; Owen et al., 2004; Hasegawa, Fujimoto, Phan et al., 2004). Similar detections of 134 two K-H instability phases are seen at Saturn's magnetopause (Masters et al., 2009; Masters 135 et al., 2010; Wilson et al., 2012; Delamere et al., 2013), and the instability is predicted for 136 Jupiter's magnetopause (Desroche 2012; Masters 2017; Zhang et al., 2018). Magnetic guide 137 field is found to stabilize K-H instability growth, therefore K-H vortices are expected mainly 138 on magnetopause flanks where magnetosheath and magnetospheric magnetic fields are either 139 parallel or antiparallel (Thomas and Winske, 1993; Miura, 1995; Eastwood et al., 2015). 140 Observations suggest K-H vortices strongly favor the parallel magnetic configuration i.e. the 141 interplanetary magnetic field (IMF) is northward (Hasegawa, Fujimoto, Phan et al., 2004; 142 Masters et al., 2010), but smaller intermittent instability growth is viable under the 143 antiparallel configuration i.e. the IMF is southward (Hwang et al., 2011). The latter scenario 144 is particularly important because Ganymede's magnetopause always maintains a near-145 antiparallel magnetic configuration due to the moon's 176° magnetic axis tilt angle and the 146 dominant southward component of the Jovian magnetic field.

147

148 There is a temptation to only use the ideal MHD theory for K-H instability assessment.149 However, observations from Mercury's magnetopause indicate that kinetic effects can also

150 play an important role in K-H instability growth. Both K-H linear waves and nonlinear 151 vortices have been observed at Mercury's magnetopause (Slavin et al., 2008; Boardsen et al., 152 2010; Sundberg et al., 2012; Liljeblad et al., 2014). But unlike other planetary cases, K-H 153 vortices are seen primarily on the dusk flank of Mercury's magnetopause (Sundberg et al., 2012; Liljeblad et al., 2014). The asymmetry is a consequence of the finite Larmor radius 154 155 (FLR) effect, a kinetic phenomenon in which gyromotions of ions inside near-magnetopause plasmas create vorticities that add to or subtract from bulk flow shear vorticity (Nagano, 156 157 1978; Nagano, 1979; Huba, 1996). The FLR effect is particularly enhanced at Mercury as its 158 magnetopause is thin enough that the gyroradii of nearby ions become significant 159 (Glassmeier & Espley, 2006; Sundberg et al., 2010; Nakamura et al., 2010; Paral & Rankin, 160 2013). As Ganymede's magnetosphere is of similar size to Mercury's, we expect a similarly 161 thin magnetopause therefore FLR effect must be considered when assessing K-H instability 162 growth.

163

164 Hence in Section 2, we will first calculate the K-H instability growth rate at Ganymede's upstream magnetopause flanks under MHD-FLR hybrid theory. Then, we will assess K-H 165 instability onset and propagation at global scale under the general ideal MHD theory in 166 Section 3. Both assessments utilize an analytical model which parametrizes plasma/magnetic 167 168 conditions along an idealized Ganymedean magnetopause surface (Kaweeyanun et al., 2020). 169 The model also assumes that no competing interactions, particularly global-scale magnetic 170 reconnection, occur during this analysis. These simplifications reduce precision of the 171 model's predictions but allow them to be obtained at minimal computational cost. In Section 172 4, we will compare our results to those on Mercury's magnetopause (where K-H vortices 173 have been observed) to discuss the potential for K-H vortex growth on Ganymede's 174 magnetopause first when reconnection effects are excluded, and later when they are included.

176 2. K-H Instability Growth Rate Under MHD-FLR Theory

Figure 1 shows a schematic diagram for K-H instability growth on Ganymede's 177 178 magnetopause flanks in a Cartesian coordinate system centered at Ganymede (GphiO) where 179 X is parallel to the ambient Jovian plasma flow, Y points toward Jupiter, and Z points 180 approximately toward Ganymede's geographical north pole. In this equatorial plane view, the 181 ambient Jovian plasma $(v_{1,0})$ enters from top of the diagram and is symmetrically deflected by 182 the magnetopause, resulting in equal Jovian-side bulk flow velocities (v_J) along both 183 magnetopause flanks. For planetary magnetopauses, the flanks are typically defined as dawn 184 and dusk where the planet rotates in the direction from the dusk flank to the dawn flank. The 185 same geometry does not apply to the Ganymedean system, however, as the Jovian plasma 186 rotates around Jupiter while the solar wind travels radially away from the Sun. Instead, the 187 rotational flow creates "near-Jupiter" and "far-Jupiter" magnetopause flanks where the 188 former lies between Ganymede and Jupiter. If we assume flank-symmetric Ganymedean-side 189 bulk flow velocities (v_G) resulting from the global-scale Dungey-type reconnection (e.g. Jia et al., 2009), then bulk flow shears ($v_{sh} = v_I - v_G$) create equal vorticities (black circular 190 191 arrows) that point southward (into page) on near-Jupiter flank and northward (out of page) on 192 far-Jupiter flank.

193

To consider the FLR effect, we choose one point along each flank where (X = 0, Z = 0). Zoom windows in Figure 1 show local plasma ion gyromotions at these equatorial flank points. Here we assume adjacent Jovian and Ganymedean magnetic fields to be directly southward and northward respectively. Since both magnetic fields never deviate beyond 45° from the Z-axis, the assumption represents a fairly typical magnetic configuration near Ganymede's magnetopause (Khurana 1997; Kivelson et al., 1998; Jia et al., 2008). Near each 200 flank point, ion gyromotions create Jovian-side (v_{i,J}) and Ganymedean-side (v_{i,G}) ion flows, where $v_{i,J} \gg v_{i,G}$ as a typical Jovian plasma ion has a much larger gyroradius and a smaller 201 gyrofrequency (shown later in Table 1). The resulting ion flow shears $(v_{i,sh} = v_{i,J} - v_{i,G})$ are 202 203 therefore significant and create equal southward vorticities (red circular arrows) on both near-Jupiter and far-Jupiter flanks. Since the plasma bulk flow and ion gyromotion-related flow 204 205 vorticities are parallel on the near-Jupiter flank but antiparallel on the far-Jupiter flank, the combined vorticity must be greater on the near-Jupiter flank, so the K-H instability should 206 grow faster on this flank as well. 207

208

209 The K-H instability can be quantified by the growth rate (γ) of its linear wave amplitudes, 210 which we calculate at each magnetopause flank point following (Nagano, 1978, 1979; 211 Sundberg et al., 2010)

$$\gamma = \sqrt{-\frac{(\rho_{G}\nu_{G} - \rho_{J}\nu_{J})^{2}}{(\rho_{G} + \rho_{J})^{2}}k^{4} - \frac{2\rho_{G}\rho_{J}}{(\rho_{G} + \rho_{J})^{2}}(v_{sh})k^{3} + \frac{\rho_{G}\rho_{J}}{(\rho_{G} + \rho_{J})^{2}}(v_{sh})^{2}k^{2} \#(1)}$$

where ρ is plasma mass density and v is gyro-viscous coefficient calculated from ion gyroradius R and gyrofrequency Ω . Subscripts "J" and "G" refer to Jovian-side and Ganymedean-side locations respectively. v_{sh} is again the cross-magnetopause bulk flow shear. Lastly, $k = \frac{2\pi}{\lambda}$ is the wavevector corresponding to linear K-H wavelength λ on the magnetopause surface.

217

Gyro-viscous coefficients and the bulk flow shear can be positive or negative, despite their listed formulas giving only positive magnitudes. At both flank points, we define $v_J > 0$ as the Jovian-side ion gyrates with northward rotation vector in Figure 1, and $v_G < 0$ as the Ganymedean-side ion gyrates with southward rotation vector. Similarly, we define $v_{sh} < 0$ on near-Jupiter flank and $v_{sh} > 0$ on far-Jupiter flank as bulk flow vorticity vectors are northward and southward there respectively. The value of each negative parameter is equal to its magnitudes multiplied by -1.

225

K-H instability can grow along a magnetopause flank only if γ is real and positive. The k⁴ 226 227 term is always negative therefore it stabilizes K-H growth at shorter wavelengths. The term depends on ρ and ν , whose values are the same between near-Jupiter and far-Jupiter flanks, 228 so the k^4 term is equal for both flanks. The k^2 term is always positive therefore it encourages 229 K-H instability growth at longer wavelengths. Since this term depends only on ρ and $(v_{sh})^2$, 230 its value is also equal for both flanks. Hence, the FLR effect arises only from the k^3 term, 231 232 whose value can be positive or negative depending on the sign of linear v_{sh} , which differs 233 between the near-Jupiter and far-Jupiter flanks.

234

235 In this study, we consider Jovian plasma to be one singly charged fluid with 14 mass-tocharge (M/Q) ratio, 60 eV temperature, and 4 cm⁻³ number density on both magnetopause 236 237 flanks (Kivelson et al., 2004). Across the magnetopause, previous studies suggest 238 Ganymedean plasma is also a singly charged fluid with 16 M/Q ratio (O⁺ dominant), 1.0 eV temperature, and 2 cm⁻³ number density on both flanks (Eviatar and Vasyliunas, 2001; Jia et 239 240 al., 2008; Jia et al., 2009). The estimated magnetic field strengths on Jovian and Ganymedean 241 sides of each magnetopause flank are 67 nT and 122 nT respectively (derived from analytical 242 model results in Figures 4e-4f later discussed in Section 3). Hence, we calculate the ion gyroradius, gyrofrequency, and gyro-viscous coefficient on both sides of the magnetopause in 243 244 Table 1. The Jovian ion gyroradius (62.91 km) is non-negligible compared to Ganymede's magnetopause current sheet thickness (<400 km from Kivelson et al., 1998), justifying 245 246 inclusion of the FLR effect in K-H instability growth rate calculations.

The ambient Jovian plasma flows at a typical speed of $v_{J,0}\approx$ 140 km/s (Williams, Mauk, & 248 249 McEntire, 1997; Williams, Mauk, McEntire, & Roelof, et al., 1997; Jia et al., 2008). As the 250 ambient plasma approaches Ganymede's magnetosphere, it first slows down near the nose of 251 the upstream magnetopause and then accelerates near the magnetopause flanks due to 252 Bernoulli's effect (e.g. Jia et al., 2009). Therefore, we consider a range of Jovian flow speed 253 between $v_I = 100 - 200$ km/s with 1 km/s resolution in this study. In comparison, the 254 antiparallel Ganymedean plasma flow speed is taken to be negligible $v_G \approx 0$ km/s. This is a viable assumption because our idealized model does not consider plasma/magnetic 255 256 interactions inside Ganymede's magnetosphere e.g. magnetic reconnection in the downstream 257 magnetotail. Hence, the bulk flow shear $v_{sh} \approx v_I$ is effectively an independent variable.

258

259 Another variable is the K-H wavelength λ . The Galileo spacecraft measures nearmagnetopause magnetic perturbation periods of 15-20 s, which gives $\lambda \sim 1050 - 1400$ km 260 assuming K-H waves propagate at $v_p \sim 0.5 v_{sh} \sim 0.5 v_J$ (Kivelson et al., 1998). However, the 261 262 K-H wavelength remains poorly constrained given lack of published plasma data during magnetopause crossings from Galileo, so we choose an extended range of $\lambda = 0 - 30,000$ 263 264 km with 1 km resolution for our study. This range is also consistent with one used in 265 Sundberg et al. (2010) K-H instability growth rate study at Mercury's magnetopause, to which we will compare our results in Section 4. 266

268 Figure 2 shows the logarithm of K-H instability growth rate at near-Jupiter and far-Jupiter 269 equatorial flank points with respect to the bulk flow shear and the logarithm of linear K-H wavelength (normalized in R_G for later Ganymede-Mercury comparison). The minimum K-H 270 271 wavelength thresholds for positive growth rate is between 10-19 km on near-Jupiter flank and 38-76 km on far-Jupiter flank. The threshold value at $v_{sh} = 100$ km/s is approximately twice 272 of value at $v_{sh} = 200$ km/s, as the K-H wavelength is inversely proportional to bulk flow 273 274 shear along the zero-growth-rate curve. At a particular flow shear speed on either flank, the 275 growth rate first rises briefly, reaching its peak only a few km after the minimum K-H 276 wavelength threshold, and then monotonically falls as λ continues to increase. The initial growth rate rise is due to significance of the k^4 term on the near-Jupiter flank and the k^3 term 277 on the far-Jupiter flank, while the subsequent fall is due to dominance of the k^2 term in the 278 growth rate expression. Both flanks have minimum growth rates of $\approx 0.01 \text{ s}^{-1}$ at longest K-H 279 wavelengths. Maximum growth rates meanwhile significantly diverge, reaching 47.89 (\approx 48) 280 s⁻¹ on near-Jupiter flank but only 6.71 (\sim 7.0) s⁻¹ on far-Jupiter flank. Typical Ganymedean K-281 H wavelengths are confined between two dashed magenta lines. Inside this range, the growth 282 rate is limited to 0.21-0.61 s⁻¹ on near-Jupiter flank and 0.20-0.60 s⁻¹ on far-Jupiter flank. 283

284

285 The growth rate asymmetry between the two flanks $\Delta \gamma = \gamma_n - \gamma_f$ is shown as a fraction of 286 the far-Jupiter value γ_f in Figure 3. Unlike the actual growth rate values, the asymmetry 287 fraction decreases with faster bulk flow shear. The asymmetry fraction grows as large as 288 $\frac{\Delta \gamma}{\gamma_f} \sim 20$ near the minimum K-H wavelength thresholds and as small as $\frac{\Delta \gamma}{\gamma_f} \sim 0.001$ at longest 289 K-H wavelengths. Typical Ganymedean wavelengths are again denoted by dashed magenta 290 lines, inside which the asymmetry fraction is $\frac{\Delta \gamma}{\gamma_f} = 0.02 - 0.06$. 292 We test the sensitivity of K-H instability growth rate to the near-magnetopause conditions by 293 changing ion M/Q ratio, temperature, and number density inputs by $\pm 50\%$ on both Jovian and 294 Ganymedean sides of the boundary. The growth rate is found most sensitive to negative changes in the three Jovian-side parameters, with the maximum rate increasing up to $\sim 100 \text{ s}^{-1}$ 295 296 (~2 factor) on the near-Jupiter flank. Within typical Ganymedean K-H wavelengths however, 297 effects of near-magnetopause conditions become effectively negligible. For the growth rate 298 asymmetry, it is difficult to determine the parameter to which the asymmetry fraction is most 299 sensitive. The maximum asymmetry value is not a meaningful measurement as it is almost 300 completely determined by numerical effects. With each parameter change, we generally find 301 that the asymmetry fraction increases/decreases by ~50% at shorter wavelengths close to minimum K-H wavelength threshold. This sensitivity is then reduced to <5% at $\lambda > \sim 100$ 302 303 km.

304

305 Implications of K-H instability growth rates on the formation of nonlinear K-H vortices, and
306 the significance of FLR effect on Ganymede's upstream magnetopause, will be revisited in
307 Section 4.

308

309 3. Assessment of K-H Instability Onset across Ganymede's Upstream Magnetopause

As discussed in Section 1, waves on Ganymede's upstream magnetopause may arise from the linear phase of K-H instability. However, the formation of linear K-H waves at Ganymede has not been assessed under fundamental plasma theory. This can be achieved by evaluating the K-H instability onset condition across Ganymede's magnetopause. Since we are
considering a global-scale situation, the ideal MHD onset condition can be used following
Masters (2017)

$$\left[\mathbf{k}\cdot\left(\mathbf{v}_{\mathbf{J}}-\mathbf{v}_{\mathbf{G}}\right)\right]^{2} > \frac{1}{\mu_{0}}\left(\frac{1}{\rho_{J}}+\frac{1}{\rho_{G}}\right)\left[\left(\mathbf{k}\cdot\mathbf{B}_{\mathbf{J}}\right)^{2}+\left(\mathbf{k}\cdot\mathbf{B}_{\mathbf{G}}\right)^{2}\right] \#(2)$$

316 where \mathbf{k} is the K-H wavevector of unit length, \mathbf{v} is bulk flow velocity vector, \mathbf{B} is magnetic field vector, ρ is plasma mass density, and $\mu_0 = 4\pi \times 10^{-7}$ H/m is the vacuum permeability 317 constant. Subscripts "J" and "G" denote Jovian and Ganymedean sides of the magnetopause 318 respectively. A point on the magnetopause surface is considered "K-H unstable" if the 319 320 inequality is satisfied. The unstable condition is favored if 1) the bulk flow shear is large, 2) 321 mass densities on both sides of the boundary are large, 3) adjacent magnetic fields are weak, 322 and 4) the K-H wavevector is parallel to the bulk flow shear and/or orthogonal to adjacent 323 magnetic fields.

324

In this study, Ganymede's magnetopause surface is produced by an analytical model whose 325 326 construction has been detailed in Kaweeyanun et al., (2020). The model domain in GphiO 327 coordinates is -4.0 < Y < 4.0 R_G and -1.0 < Z < 1.0 R_G with 0.01 R_G resolution in each dimension. The model accounts for Ganymede's up-down movement in the Jovian plasma 328 329 sheet via Jupiter's east longitude parameter ϕ . The magnetopause is north-south symmetric when Ganymede lies at the center of the Jovian plasma sheet ($\phi = 248^\circ$), and gains largest 330 331 asymmetry when the moon reaches its highest point ($\phi = 158^\circ$) and lowest point ($\phi = 338^\circ$) 332 in the plasma sheet. We will consider these three specific cases when evaluating the K-H 333 instability onset condition.

335 The model then parametrizes plasma and magnetic parameters on both sides of the 336 magnetopause. Figure 4 (adapted from Kaweevanun et al., 2020) demonstrates this process for the case when $\phi = 248^\circ$. The magnetopause is first projected onto a Y-Z plane (bulk 337 flow into page) and the surface X-coordinates shown in Figure 4a. As expected, the 338 339 magnetopause curves downstream (X value increasing) toward the flanks, where the 340 equatorial flank points used for the K-H instability growth rate calculations in Section 2 are 341 dotted in red. Two dashed lines denote boundaries between open-field and closed-field 342 regions.

343

The ambient Jovian plasma is assumed to flow at $v_{J,0}\approx 140$ km/s along the X-direction for 344 all Ganymede positions (Jia et al., 2008). Figures 4b depicts plasma bulk flow velocity (v_J) 345 on the Jovian-side magnetopause for $\phi = 248^\circ$. The flow collides with the magnetopause 346 and the Jovian-side speed (v_J) is parametrized as a sine function of the flaring angle between 347 348 the local magnetopause normal and the ambient flow direction (Kaweeyanun et al., 2020). Hence, the flow speed is slower near the subflow point (Y = 0, Z = 0) where the collision is 349 350 head-on, and higher along the flanks where the flow is less impeded by the magnetopause. Normalized arrows indicate Jovian-side flow directions consistent with plasma traversing 351 352 around Ganymede along the magnetopause surface (Kaweeyanun et al., 2020).

353

The ambient Jovian plasma mass density depends on Ganymede's position in the plasma sheet, maximized at $\rho_{J,0} = 56$ amu/cm⁻³ when $\phi = 248^{\circ}$ and minimized at $\rho_{J,0} = 28$ amu/cm⁻³ when $\phi = 158^{\circ}$, 338° (Kivelson et al., 2004; Jia et al., 2008). Figure 4c shows the Jovian-side mass density ($\rho_{\rm J}$) when $\phi = 248^{\circ}$. The Jovian-side mass density is parametrized as a cosine function of the flaring angle with a positive offset equal to the ambient density, as the plasma gains density from magnetopause collision (Kaweeyanun et al., 2020). The density is highest near the subflow point where head-on collision creates largest plasma compression, and lowest near the flanks where the compression is negligible. The value $\rho_{\rm J} \approx 56$ amu/cm³ at the flanks is consistent with mass density used in Section 2.

363

The combined thermal and energetic plasma pressure of the ambient Jovian plasma is $P_{J,0} = 3.8$ nPa when $\phi = 248^{\circ}$ and $P_{J,0} = 1.9$ nPa when $\phi = 158^{\circ}, 338^{\circ}$ (Kivelson et al. 2004; Jia et al., 2008). Figure 4d shows the Jovian-side plasma pressure (P_J) when $\phi = 248^{\circ}$. Like the mass density, the pressure increase from near-magnetopause compression is parametrized as a cosine relation of the flaring angle and added to the ambient values, resulting in higher pressure near the subflow point and lower pressure along the flanks (Kaweeyanun et al., 2020).

371

In our model, the ambient magnetic field carried by the Jovian plasma has strength $B_{I,0} = 70$ 372 nT when $\phi = 248^{\circ}$ and $B_{J,0} = 105$ nT when $\phi = 158^{\circ}, 338^{\circ}$ (Khurana, 1997; Jia et al., 373 2008). Assuming negligible B_{J,0,x} component (Jia et al., 2008), the ambient Jovian field 374 375 strength is distributed between $B_{J,0,y}$ and $B_{J,0,z}$ components such that the field points along negative Z-direction when $\phi = 248^\circ$, and deviates $\approx 45^\circ$ from negative Z-direction when 376 $\phi = 158^\circ$, 338° (Jia et al., 2008; Kaweeyanun et al., 2020). The magnetic field is compressed 377 378 near the magnetopause similar to the mass density and plasma pressure, so the Jovian-side 379 field (\mathbf{B}_{J}) is strongest near the subflow point and weakest along the flanks as shown in Figure

4e when $\phi = 248^{\circ}$. The magnetic field strength is $B_J \approx 67$ nT at both equatorial flank points. The pressure conservation method used to determine the Jovian-side field strength is previously discussed in Kaweeyanun et al., (2020). The Jovian-side field direction (normalized arrows) is similar to the ambient direction, but additionally constrained to be parallel to the magnetopause surface (Kaweeyanun et al., 2020).

385

386 Plasma inside Ganymede's magnetosphere exerts negligible pressure due to its relatively cold temperature (Jia et al., 2008). Therefore, Ganymede's magnetic field is the primary 387 388 contributor in balancing the combined Jovian-side plasma and magnetic pressures adjacent to 389 the magnetopause. This allows computation of the Ganymedean-side magnetic field (\mathbf{B}_{G}) shown in Figure 4f when $\phi = 248^{\circ}$. As expected, the Ganymedean-side field strength is 390 391 strongest near the subflow point and weakest along the flanks. The magnetic field strength is $B_G \approx 122$ nT at both equatorial flank points. The field direction (normalized arrows) is 392 393 required to be approximately dipolar and parallel to the magnetopause (Kaweeyanun et al., 394 2020). The magnetic field points northward in the closed-field region and southward in the 395 open-field region. The Ganymedean-side mass density and bulk plasma flow speed are taken be uniform with magnitudes $\rho_G = 32$ amu/cm⁻³ and $v_G = 0$ km/s respectively, consistent 396 397 with information used in Section 2.

398

399 Once we obtain the magnetopause conditions exemplified in Figure 4 for all three Ganymede 400 positions, we can evaluate the K-H instability onset condition in the closed-field region 401 where the instability can potentially influence Ganymede's magnetospheric dynamics. At 402 each magnetopause surface point, we first assess the onset condition with the K-H 403 wavevector parallel to the bulk flow shear ($\mathbf{k} \parallel \mathbf{v}_{J} - \mathbf{v}_{G}$), and then reassess the condition after 404 every 1° wavevector rotation. Two criteria are required for a point to be considered K-H 405 unstable. First, the point must have at least one wavevector orientation that satisfies the onset 406 inequality. Second, the point must have at least four neighboring points that satisfy the first 407 criterion. The latter criterion removes the "isolated unstable points" (i.e. inequality satisfied 408 by a smallest margin for only one wavevector orientation) where the K-H instability 409 effectively cannot grow.

411 At each K-H unstable point, we calculate the zero-momentum (center-of-mass) frame
412 velocity along which the K-H linear wave propagates following

$$\mathbf{v_p} = \left(\frac{\rho_{\rm J}}{\rho_{\rm J} + \rho_{\rm G}}\right) \mathbf{v_J} \#(3)$$

413 where the parameters retain their usual definitions. Since we consider one cross-414 magnetopause volume containing both Jovian-side and Ganymedean-side plasmas, mass 415 densities can substitute for masses in the velocity expression. The equation indicates that K-H 416 waves always propagate in same direction as the external Jovian-side bulk flow.

417

Figure 5 shows the K-H instability onset condition assessment in the closed-field region for (a) $\phi = 248^{\circ}$, (b) $\phi = 158^{\circ}$, and (c) $\phi = 338^{\circ}$. Magnetopause conditions are K-H unstable in the colored regions and K-H stable in the white regions. The color scale and normalized arrows describe zero-momentum frame speed and direction respectively. Figure 5a indicates that when Ganymede lies at the center of Jovian plasma sheet, its magnetopause is largely K- 423 H unstable except the areas immediately north/south of the subflow point. The unstable area 424 includes the magnetopause flanks where the K-H instability growth rates are computed in 425 Section 2 (red dots). The zero-momentum frame speed ranges from <1 km/s closest to the 426 subflow point up to 89 km/s far along the magnetopause flanks.

427

Figures 5b-5c show sizable reductions in K-H unstable areas as Ganymede is at highest and lowest points relative to the plasma sheet's center. K-H waves can form only inside narrow strips along magnetopause flanks beyond $|Y| > 2 R_G$. The zero-momentum frame speed smaller ranges 50-66 km at these Ganymede positions. We see that the K-H waves can still propagate toward the magnetopause flanks, but with evident effects from the north-south magnetopause asymmetry.

434

435 There are two factors why Ganymede's magnetopause become less K-H unstable when 436 $\phi = 158^\circ$, 338°. First, adjacent magnetic fields are 50% stronger compared to when $\phi =$ 437 248°, while Jovian-side mass densities are 50% less dense. Both parameter changes increase 438 the right-hand side of the K-H onset condition thus raising the threshold for K-H instability. 439 The K-H unstable area size is much more sensitive to magnetic field strengths than mass densities as the onset threshold is proportional to $|B_J|^2$ and $\frac{1}{\rho_I}$ respectively. Second, the north-440 south magnetopause asymmetry means the bulk flow shear is no longer near-orthogonal to 441 442 the adjacent magnetic fields (which are always strongly antiparallel to each other). Consequently, there exist fewer K-H wavevector orientations that are simultaneously parallel 443 444 to the bulk flow shear and orthogonal to the adjacent magnetic fields, hence the K-H onset 445 condition is less likely to be satisfied. Sensitivity tests suggest that both factors have

446 significant impacts on K-H instability onset, but a quantitative impact comparison is difficult447 due to the approximative nature of our analytical model.

448

449 The K-H instability onset is impacted not only by Ganymede's spatial position, but also temporal changes in the Jovian plasma sheet. Although the analytical model assumes steady-450 451 state conditions, temporal effects can be mimicked by changing plasma parameters without 452 changing Ganymede's position. Figure 6 illustrates K-H instability onset assessment when 453 the Jovian-side flow speed and mass densities vary by $\pm 50\%$ (magnetic field strengths 454 unchanged due to fixed Ganymede position). The size of K-H unstable area is much more sensitive to the Jovian-side flow speed (Figures 6a-6b) than mass density (Figures 6c-6d), 455 456 because the left-hand side of the onset condition linearly depends on v_J. But unlike adjacent 457 magnetic fields, increasing the flow speed enlarges K-H unstable areas. Interestingly, the impact of -50% flow speed (Figure 6a) is significantly greater than that of +50% flow speed 458 459 (Figure 6b). The asymmetry occurs because the bulk flow shear is almost parallel to adjacent magnetic fields directly above/below the subflow point, so the magnetopause is highly K-H 460 461 stable in these regions.

462

When $\phi = 248^{\circ}$, Figure 5a data shows that K-H linear waves propagate at $v_{cm} \sim 0.65 v_{sh}$ inside the K-H unstable flank regions. When $\phi = 158^{\circ}$, 338°, Figures 5b-5c data show the propagation speed is $v_{cm} \sim 0.48 v_{sh}$. These values indicate that the assumption $v_p =$ $v_{cm} \sim 0.5 v_{sh}$ used to estimate the K-H instability wavelength in Section 2 is reasonable.

469 The MHD-FLR theory has previously been applied to calculate K-H instability growth rates 470 at Mercury's equatorial magnetopause flank points (Sundberg et al., 2010). The calculation 471 assumes a directly northward IMF, in which case global magnetic reconnection is minimized. 472 Hence, the Sundberg et al. (2010) model can be compared to our study in Section 2, which 473 also consider Ganymedean K-H instability growth rates without reconnection effects despite 474 the southward Jovian magnetic field orientation. Similar to Figure 2, the Hermean growth 475 rate in Figure 6 of Sundberg et al. (2010) briefly rises and then falls with increasing K-H 476 wavelength for each bulk flow shear speed considered. The growth rates at Mercury's dawn 477 magnetopause flank point are enhanced and of comparable magnitudes to those at 478 Ganymede's near-Jupiter flank point. However, the growth rates on Mercury's dusk flank 479 point are ~1.5 orders of magnitude smaller than those at Ganymede's far-Jupiter flank point. 480 The minimum K-H wavelength thresholds also show larger asymmetry between flanks at 481 Mercury (>1,000 km) than Ganymede (~50 km). Both growth rate and minimum threshold asymmetries suggest a stronger FLR effect at Mercury's magnetopause. 482

484 Given their similar scales ($R_G \sim R_M$), the largely comparable K-H instability growth rates 485 between Mercury and Ganymede seem to suggest similar levels of K-H vortex growths. 486 However, this depends on variabilities of typical K-H wavelengths and external magnetic 487 field orientations. On the one hand, K-H vortices grow fastest at shortest K-H wavelengths, 488 therefore a typical Ganymedean wavelength range of 1,050-1,400 km would result in fewer 489 vortices at Ganymede than Mercury, given the latter's estimated wavelength range of 500-490 5,000 km (Nakamura et al., 2010). On the other hand, Mercury's effective K-H instability 491 growth rates are much lower than MHD-FLR values due to the large range of variabilities of the IMF orientation, which is not the case for Ganymede because the Jovian magnetic field is
always strongly southward. What is certain, however, is that K-H vortex growth at
Ganymede's magnetopause flank points cannot be ruled out given the evidence of Mercury's
K-H vortices in Section 1.

496

497 The MHD-FLR theory does not account for the impact of non-negligible magnetopause current sheet thickness on K-H instability growth. Hence, we also consider Mercury's growth 498 499 rates that are derived from a two-dimensional kinetic simulation (Nakamura et al., 2010), 500 specifically when the pre-instability magnetopause thickness is similar to the local inertial 501 length as this is the situation at Ganymede's magnetopause (Kaweeyanun et al., 2020). In this 502 case, Figure 7 in Nakamura et al. (2010) shows that the Hermean growth rates exhibit rise-503 and-fall relationships with K-H wavelengths with significantly less prominent peaks and a 504 noticeable dawn-dusk FLR effect, consistent with MHD-FLR results. However, a more 505 quantitative growth rate comparison is not recommended due to differences between MHD-506 FLR and kinetic theories.

507

As an alternative to Mercury comparisons, Ganymede's K-H instability growth rate can be
considered as a parameter controlling K-H wave amplitude such that

$$A_{f} = A_{i} e^{\gamma t} \#(4)$$

where A_i is the initial amplitude before K-H instability growth and A_f is the final amplitude after time t. A very large K-H wave amplitude is likely to, but not necessarily, induce a K-H vortex as long as the wave has not propagated past Ganymede's magnetotail. We estimate the 513 distance (in R_G) a K-H wave travels before its amplitude reaches the K-H vortex threshold, taken to be $A_f = 100$ nT, in Table 2 using initial amplitudes $A_i = [1, 5, 10, 15, 20]$ nT and 514 growth rates $\gamma = [0.01, 0.1, 1, 10] \text{ s}^{-1}$. A K-H wave is assumed to propagate at $v_p = 85 \text{ km/s}$ 515 (from Figure 5a) during its amplitude growth. Ganymede's magnetotail length from 516 517 magnetopause flank points is ~7.5-9.0 R_G (Jia, Kivelson et al., 2010). Table 2 suggests that a 518 K-H wave will become a vortex unless both the initial amplitude and the growth rate are small (A_i < 5 nT and $\gamma = 0.01$ s⁻¹). Given values inferred from Galileo measurements 519 $(A_i \approx 10 - 20 \text{ nT}, \gamma = 0.20 - 0.61 \text{ s}^{-1})$ in Kivelson et al., (1998), this simplistic application 520 of K-H instability theory also suggests that formation of K-H vortices is viable at 521 522 Ganymede's equatorial magnetopause flank points.

523

524 The K-H instability onset assessment in Figure 5 shows that the plasma and magnetic field 525 conditions along Ganymede's magnetopause flanks will lead to K-H waves at all latitudes 526 irrespective of Ganymede's spatial positions relative to Jupiter's plasma sheet. Throughout 527 these flank K-H unstable regions, local magnetic shear angles are close to 180° and the bulk 528 flow shears are nearly orthogonal to Jovian/Ganymedean magnetic fields (Kaweeyanun et al., 529 2020). Consequently, magnetic and plasma configurations are similar to Figure 1 at all flank latitudes for all Ganymede spatial positions, so we can adopt K-H instability growth rates in 530 531 Section 2 throughout Ganymede's magnetopause flank regions. Figure 5 also indicates that K-H instability occurs more frequently (larger K-H unstable area) when Ganymede lies at 532 center of the Jovian plasma sheet. This is opposite from global-scale magnetic reconnection 533 534 which occurs more frequently when Ganymede lies at extreme orbital positions (Kaweeyanun et al., 2020). 535

537 This raises the question of relative strengths between K-H instability and global reconnection 538 in cross-magnetopause energy transport, particularly whether they alternate according to Ganymede's position relative to the Jovian plasma sheet. Although this question has been 539 540 investigated for planetary magnetopauses by Masters (2018), the same method does not apply 541 for Ganymede since the moon does not interact with the solar wind. Hence to answer this 542 question, we evaluate how Ganymede's K-H instability growth interacts with global 543 reconnection. Under southward external magnetic field, reconnection events can disrupt K-H 544 instability growth by altering near-magnetopause plasma/magnetic conditions (Nakamura et 545 al., 2020). We consider as an analogue the case of Mercury's magnetopause when the IMF is southward. In-situ observations from the MESSENGER mission find that only 11% of 546 547 Mercury's K-H vortices occur under southward IMF (Liljeblad et al., 2014), indicating a 548 suppressive impact of Hermean reconnection on K-H instability growth. Mercury's estimated 549 reconnection electric field strength is ~0.3-3 mV/m (Gershman et al., 2016), which is 550 exceeded by Ganymede's typical values of 2 - 20 mV/m (Kaweeyanun et al., 2020; Zhou et 551 al., 2020). As the two magnetospheres are similar in size, reconnection rates can be compared directly via electric field strengths. Therefore, reconnection at Ganymede occurs at higher 552 553 rates and should have an even larger suppressive impact on K-H instability growth than at 554 Mercury, especially since the Jovian magnetic field is permanently southward at Ganymede. 555 Consequently, we expect few K-H vortices at Ganymede's magnetopause once global 556 reconnection is taken into account, and the latter interaction should be the dominant mean of 557 cross-magnetopause energy transport for all orbital positions of Ganymede.

558

In a Dungey-type plasma cycle, magnetic reconnection is also expected in the downstream
 magnetotail. According to numerical simulations, downstream reconnection generates bulk

plasma flow speed $v_G = 20 - 50$ km/s along the Ganymedean-side magnetopause flank, in direction antiparallel to the Jovian-side flow (e.g. Jia et al., 2009). The incorporation of finite v_G reduces the bulk flow shear and thus the K-H instability growth rate. However, both the growth rates and minimum K-H wavelength thresholds remain within the same orders of magnitude as the results in Section 3. Hence, the introduction of downstream reconnection would not change the main conclusions drawn.

567

568 Our discussion does not consider impacts of adjacent magnetic field realignments in response 569 to initial K-H instability growth, which can introduce a stabilizing guide effect, or other 570 disruptive factors such as the tearing-mode instability (Chen et al., 1997), pressure rarefaction 571 regions near the magnetopause (Miura, 1995), and ion cyclotron waves (Volwerk et al., 1999; 572 Volwerk et al., 2013). However, these factors are potential subjects for future research on K-573 H instability growth along Ganymede's upstream magnetopause.

574

575 **5.** Conclusion

576 Dynamics within Ganymede's unique magnetosphere are thought to be driven primarily by energy-transfer interactions on the moon's upstream magnetopause. One such interaction is 577 578 the Kelvin-Helmholtz (K-H) instability particularly during its turbulent nonlinear vortex 579 phase. In this paper, we conduct the first assessment of K-H instability growth on 580 Ganymede's magnetopause, using a previously established analytical model to capture the 581 plasma and magnetic conditions near the boundary (Kaweeyanun et al., 2020). The 582 assessment occurs in isolation from global magnetic reconnection effects and is divided into 583 two steps. First, the K-H instability growth rate is calculated at one equatorial point along

each of Ganymede's two magnetopause flanks via a modified magnetohydrodynamic with finite Larmor effect (MHD-FLR) theory, which accounts for effects of large Jovian plasma ion gyroradii. Then, we evaluate the ideal MHD K-H instability onset condition to reveal the extent of instability growth at global scale.

588

Ganymede's K-H instability growth rate has an estimated range of $\gamma \approx 0.01 - 48 \text{ s}^{-1}$, with 589 slightly faster growth rates at the near-Jupiter equatorial flank point. These values are 590 591 comparable in magnitude to those along Mercury's dawn magnetopause flank, which seems 592 to suggest a similar level of K-H vortex growth between the two bodies, but this remains 593 inconclusive due to poorly constrained wavelengths of linear K-H waves at Ganymede and 594 highly variable interplanetary magnetic field (IMF) orientation at Mercury. Meanwhile, the 595 inter-flank growth rate asymmetry due to the FLR effect is expected to be less pronounced at 596 Ganymede than Mercury.

597

598 The K-H instability onset assessment reveals the entire low-to-mid latitude portion of 599 Ganymede's magnetopause to be largely favorable for instability growth, particularly near 600 the magnetopause flank regions. K-H waves at these locations should grow at similar rates to 601 those at equatorial flank points given similar plasma/magnetic configurations across 602 Ganymede's magnetopause flanks. The instability growth is expected to be more prevalent 603 when Ganymede is at center of the Jovian plasma sheet, which is opposite from global 604 reconnection which favors conditions when Ganymede is at its highest/lowest points relative 605 to the plasma sheet. We determine the relative strengths between the two phenomena by 606 considering their interaction using Mercury's magnetopause as an analogue case. K-H vortex

growth is expected to be strongly suppressed by frequent reconnection events, hence the
latter interaction should be the dominant energy-transfer mechanism on Ganymede's
upstream magnetopause (Jia, Walker et al., 2010; Kaweeyanun et al., 2020; Zhou et al.,
2020).

611

The conclusions discussed above are largely qualitative due to approximations used in the MHD-FLR theory and Ganymede's analytical model, and our analysis does not account for time variability in K-H instability growth rates. Future work in this area may focus on quantitative analysis of interactions between magnetic reconnection and K-H instability events, and the effects of temporal dynamics on both types of energy-transfer interactions, both of which can help inform the upcoming JUpiter ICy moon Explorer (JUICE) mission.

618

619 Acknowledgements

NK is supported by a Royal Society PhD Studentship, and AM is supported by a Royal
Society University Research Fellowship. Derived data in Figures 2-6 is available in the
Imperial College High Performance Computing Service Data Repository (Kaweeyanun,
2020b).

624 **Reference**

625	Anderson, J. D., Lau, E. L., Sjogren, W. L., Schubert, G., & Moore, W. B. (1996).
626	Gravitational constraints on the internal structure of Ganymede. Nature, 384 (6609), 541-
627	543. https://doi.org/10.1038/384541a0
628	
629	Bagenal, F., Wilson, R. J., Siler, S., Paterson, W. R., & Kurth, W. S. (2016). Survey of
630	Galileo plasma observations in Jupiter's plasma sheet. Journal of Geophysical Research:
631	Planets, 121 (5), 871-894. https://doi.org/10.1002/2016JE005009
632	
633	Boardsen, S. A., Sundberg, T., Slavin, J. A., Anderson, B. J., Korth, H., Solomon, S. C., &
634	Blomberg, L. G. (2010). Observations of Kelvin-Helmholtz waves along the dusk-side
635	boundary of Mercury's magnetosphere during Messenger's third flyby. Geophysical
636	Research Letters, 37 (12). https://doi.org/10.1029/2010GL043606
637	
638	Chaston, C., Wilber, M., Mozer, F., Fujimoto, M., Goldstein, M., Acuña, M., Fazakerley,
639	A. (2007, 11). Mode conversion and anomalous transport in kelvin-helmholtz vortices and
640	kinetic alfvén waves at the earth's magnetopause. Physical review letters, 99, 175004.
641	http://doi.org/10.1103/PhysRevLett.99.175004
642	

643	Chen, Q., Otto, A., & Lee, L. C. (1997). Tearing instability, Kelvin-Helmholtz instability,
644	and magnetic reconnection. Journal of Geophysical Research: Space Physics, 102 (A1), 151-
645	161. https://doi.org/10.1029/96JA03144
646	
647	Collinson, G., Paterson, W. R., Bard, C., Dorelli, J., Glocer, A., Sarantos, M., & Wilson, R.

648 (2018). New results from Galileo's first flyby of Ganymede: Reconnection-driven flows at

the low-latitude magnetopause boundary, crossing the cusp, and icy ionospheric escape.

650 Geophysical Research Letters, 45(8), 3382–3392. <u>https://doi.org/10.1002/2017GL075487</u>

651

652	Delamere,	P.	A.,	Wilson,	R.	J.,	Eriksson,	S.,	&	Bagenal,	F.	(2013,	2020/07/08)). I	Magnetic

653 signatures of kelvin-helmholtz vortices on Saturn's magnetopause: Global survey. Journal of

654 Geophysical Research: Space Physics, 118 (1), 393–404.

655 <u>https://doi.org/10.1029/2012JA018197</u>

656

Desroche, M., Bagenal, F., Delamere, P. A., & Erkaev, N. (2012). Conditions at the expanded
Jovian magnetopause and implications for the solar wind interaction. Journal of Geophysical
Research: Space Physics, 117(A7). https://doi.org/10.1029/2012JA017621

660

661 Dungey, J. (1955). Electrodynamics of the outer atmosphere. In Physics of the ionosphere,

report of the conference held at the cavendish laboratory. Cambridge: The Physical Society.

664	Eastwood, J. P., Hietala, H., Toth, G., Phan, T. D., & Fujimoto, M. (2015). What controls the
665	structure and dynamics of Earth's magnetosphere? Space Science Reviews, 188 (1), 251-
666	286. <u>https://doi.org/10.1007/s11214-014-0050-x</u>

Eviatar, A., M. Vasyliūnas, V., & A. Gurnett, D. (2001). The ionosphere of Ganymede.
Planetary and Space Science, 49(3), 327–336. <u>https://doi.org/10.1016/S0032-0633(00)00154-</u>
<u>9</u>

671

672	Fairfield, D. H.,	Otto, A.,	Mukai, T.,	Kokubun.	S., Lepping	. R. P.	. Steinberg.	J. T.,
				11011000011,	~, _, _,	,	, ~	

673 Yamamoto, T. (2000). Geotail observations of the Kelvin-Helmholtz instability at the

- 674 equatorial magnetotail boundary for parallel northward fields. Journal of Geophysical
- 675 Research: Space Physics, 105 (A9), 21159–21173. https://doi.org/10.1029/1999JA000316

- 677 Frank, L. A., Paterson, W. R., Ackerson, K. L., & Bolton, S. J. (1997). Outflow of hydrogen
- 678 ions from Ganymede. Geophysical Research Letters, 24 (17), 2151–2154.
- 679 <u>https://doi.org/10.1029/97GL01744</u>
- 680
- 681 Gershman, D. J., Dorelli, J. C., DiBraccio, G. A., Raines, J. M., Slavin, J. A., Poh, G., &
- 682 Zurbuchen, T. H. (2016). Ion-scale structure in Mercury's magnetopause reconnection
- diffusion region. Geophysical Research Letters, 43 (12), 5935–5942.
- 684 <u>https://doi.org/10.1002/2016GL069163</u>

686	Glassmeier, KH., & Espley, J. (2006). ULF waves in planetary magnetospheres (Vol. 169;
687	K. Takahashi, Ed.). American Geophysical Union https://doi.org/10.1029/169GM22
688	
689	Grasset, O., Dougherty, M. K., Coustenis, A., Bunce, E., Erd, C., Titov, D. V., Van Hoolst,
690	T. (2013). JUpiter ICy moons Explorer (JUICE): An ESA mission to orbit Ganymede and to
691	characterise the Jupiter system. Planetary and Space Science, 78, 1–21.
692	http://doi.org/10.1016/j.pss.2012.12.002
693	
694	Gurnett, D. A., Kurth, W. S., Roux, A., Bolton, S. J., & Kennel, C. F. (1996). Evidence for a
695	magnetosphere at Ganymede from plasma-wave observations by the Galileo spacecraft.
696	Nature, 384 (6609), 535–537. <u>https://doi.org/10.1038/384535a0</u>
697	
698	Hasegawa, H., Fujimoto, M., Phan, T. D., Rème, H., Balogh, A., Dunlop, M. W.,
699	TanDokoro, R. (2004). Transport of solar wind into Earth's magnetosphere through rolled-up

- 700 Kelvin–Helmholtz vortices. Nature, 430(7001), 755–758.
- 701 <u>https://doi.org/10.1038/nature02799</u>

- 703 Huba, J. (1996). The Kelvin-Helmholtz instability: Finite Larmor radius
- 704 magnetohydrodynamics. Geophysical Research Letters Geophysical Research Letters, 23.
- 705 <u>http://doi.org/10.1029/96GL02767</u>

⁷⁰²

707	Hwang, K. J., Kuznetsova, M. M., Sahraoui, F., Goldstein, M. L., Lee, E., & Parks, G. K.
708	(2011). Kelvin-Helmholtz waves under southward interplanetary magnetic field. Journal of
709	Geophysical Research: Space Physics, 116 (A8). https://doi.org/10.1029/2011JA016596
710	
711	Jia, X., Kivelson, M. G., Khurana, K. K., & Walker, R. J. (2010). Magnetic fields of the
712	satellites of Jupiter and Saturn. Space Science Reviews, 152(1), 271-305.
713	https://doi.org/10.1007/s11214-009-9507-8
714	
715	Jia, X., Walker, R. J., Kivelson, M. G., Khurana, K. K., & Linker, J. A. (2008). Three-
716	dimensional MHD simulations of Ganymede's magnetosphere. Journal of Geophysical
717	Research: Space Physics, 113(A6). https://doi.org/10.1029/2007JA012748
718	
719	Jia, X., Walker, R. J., Kivelson, M. G., Khurana, K. K., & Linker, J. A. (2009). Properties of
720	Ganymede's magnetosphere inferred from improved three-dimensional MHD simulations.
721	Journal of Geophysical Research: Space Physics, 114 (A9).
722	https://doi.org/10.1029/2009JA014375
723	
724	Kaweeyanun, N. (2020b). (Supplementary Data) Analytical assessment of Kelvin-Helmholtz
725	instability growth at Ganymede's upstream magnetopause. Version 1.0. Imperial College

- 726 High Performance Computing Service Data Repository.
- 727 <u>http://www.doi.org/10.14469/hpc/7399</u>. Accessed 21 September 2020.

- 729 Kaweeyanun, N., Masters, A., & Jia, X. (2020). Favorable conditions for magnetic
- reconnection at Ganymede's upstream magnetopause. Geophysical Research Letters, 47 (6),
- 731 e2019GL086228. <u>https://doi.org/10.1029/2019GL086228</u>

732

- 733 Khurana, K. K. (1997). Euler potential models of Jupiter's magnetospheric field. Journal of
- 734 Geophysical Research: Space Physics, 102(A6), 11295–11306.
- 735 <u>https://doi.org/10.1029/97JA00563</u>
- 736
- 737 Kivelson, M., Bagenal, F., Kurth, W., Neubauer, F., Paranicas, C., & Saur, J. (2004).
- 738 Magnetospheric interactions with satellites (Vol. 1; F. Bagenal, T. Dowling, & W.
- 739 McKinnon, Eds.). Cambridge University Press.

740

- 741 Kivelson, M. G., Khurana, K. K., Russell, C. T., Walker, R. J., Warnecke, J., Coroniti, F. V.,
- 742 ... Schubert, G. (1996). Discovery of Ganymede's magnetic field by the Galileo spacecraft.
- 743 Nature, 384 (6609), 537–541. <u>https://doi.org/10.1038/384537a0</u>

- 745 Kivelson, M. G., Khurana, K. K., & Volwerk, M. (2002). The permanent and inductive
- 746 magnetic moments of Ganymede. Icarus, 157 (2), 507–522.

747 https://doi.org/10.1006/icar.2002.6834

748

- 749 Kivelson, M. G., Warnecke, J., Bennett, L., Joy, S., Khurana, K. K., Linker, J. A., ...
- 750 Polanskey, C. (1998). Ganymede's magnetosphere: Magnetometer overview. Journal of
- 751 Geophysi- cal Research: Planets, 103 (E9), 19963–19972. <u>https://doi.org/10.1029/98JE00227</u>

752

- 753 Liljeblad, E., Sundberg, T., Karlsson, T., & Kullen, A. (2014). Statistical investigation of
- 754 Kelvin-Helmholtz waves at the magnetopause of Mercury. Journal of Geophysical Research:
- 755 Space Physics, 119(12), 9670–9683. https://doi.org/10.1002/2014JA020614

756

- 757 Masters, A. (2017). Model-based assessments of magnetic re- connection and Kelvin-
- 758 Helmholtz instability at Jupiter's magnetopause. Journal of Geophysical Research: Space

759 Physics, 122 (11), 11,154–11,174. <u>https://doi.org/10.1002/2017JA024736</u>

760

- 761 Masters, A., Achilleos, N., Bertucci, C., Dougherty, M. K., Kanani, S. J., Arridge, C. S., ...
- Coates, A. J. (2009). Surface waves on Saturn's dawn flank magnetopause driven by the
- 763 Kelvin–Helmholtz instability. Planetary and Space Science, 57 (14), 1769–1778.
- 764 <u>https://doi.org/10.1016/j.pss.2009.02.010</u>

766	Masters, A	., Achilleos,	N., Kivelson	. M. G.,	Sergis, N.,	Dougherty.	M. K.,	Thomsen,	M. F., .

- 767 . . Coates, A. J. (2010). Cassini observations of a Kelvin-Helmholtz vortex in Saturn's outer
- 768 magnetosphere. Journal of Geophysical Research: Space Physics, 115(A7).
- 769 <u>https://doi.org/10.1029/2010JA015351</u>

771	Matsumoto,	Y., & Hoshino,	M. (2004).	Onset of tu	rbulence i	induced by	a Kelvin-	Helmholtz
-----	------------	----------------	------------	-------------	------------	------------	-----------	-----------

vortex. Geophysical Research Letters, 31(2). <u>https://doi.org/10.1029/2003GL018195</u>

773

774	Matsumoto, Y., & Hoshino, M. (2006). Turbulent mixing and transport of collisionless
775	plasmas across a stratified velocity shear layer. Journal of Geophysical Research: Space
776	Physics, 111(A5). https://doi.org/10.1029/2004JA010988
777	
778	Miura, A. (1982). Nonlinear evolution of the magnetohydrodynamic Kelvin-Helmholtz
779	instability. Phys. Rev. Lett., 49, 779–782. <u>http://doi.org/10.1103/PhysRevLett.49.779</u>

780

Miura, A. (1995). Dependence of the magnetopause Kelvin-Helmholtz instability on the
orientation of the magnetosheath magnetic field. Geophysical Research Letters, 22(21),
2993–2996. <u>https://doi.org/10.1029/95GL02793</u>

- 785 Nagano, H. (1978). Effect of finite ion Larmor radius on the Kelvin–Helmholtz instability.,
- 786 20(2), 149-160. <u>http://doi.org/10.1017/S0022377800021450</u>

- 788 Nagano, H. (1979). Effect of finite ion Larmor radius on the Kelvin-Helmholtz instability of
- the magnetopause. Planetary and Space Science, 27(6), 881–884.
- 790 https://doi.org/10.1016/0032-0633(79)90013-8

791

- 792 Nakamura, T., Fujimoto, M., & Otto, A. (2006). Magnetic reconnection induced by kelvin-
- helmholtz instability and the formation of the low-latitude boundary layer. Geophysical
- 794 Research Letters GEOPHYS RES LETT, 331. <u>http://doi.org/10.1029/2006GL026318</u>

795

- 796 Nakamura, T., Fujimoto, M., & Otto, A. (2008). Structure of an mhd-scale kelvin-helmholtz
- 797 vortex: Two-dimensional two-fluid simulations including finite electron inertial effects.
- Journal of Geophysical Research: Space Physics, 113 (A9).
- 799 <u>http://doi.org/10.1029/2007JA012803</u>
- 800
- 801 Nakamura, T., Hayashi, D., Fujimoto, M., & Shinohara, I. (2004). Decay of mhd-scale
- 802 kelvin-helmholtz vortices mediated by parasitic electron dynamics. Physical review letters,

803 92, 145001. <u>http://doi.org/10.1103/Phys- RevLett.92.145001</u>

805 Nak	amura, T.	, Hasegawa,	Н., а	& Shine	ohara, I.	(2010)	. Kinetic	effects	on the	Kelvin-
---------	-----------	-------------	-------	---------	-----------	--------	-----------	---------	--------	---------

- 806 Helmholtz instability in ion-to-magnetohydrodynamic scale transverse velocity shear layers:
- 807 Particle simulations. Physics of Plasmas, 17. <u>http://doi.org/10.1063/1.3385445</u>

- 809 Nakamura, T. K. M., Plaschke, F., Hasegawa, H., Liu, Y. H., Hwang, K. J., Blasl, K. A., &
- 810 Nakamura, R. (2020). Decay of kelvin- helmholtz vortices at the earth's magnetopause under
- 811 pure southward imf conditions. Geophysical Research Letters, 47 (13), e2020GL087574.
- 812 <u>https://doi.org/10.1029/2020GL087574</u>

813

- 814 Neubauer, F. (1998). The sub-Alfvenic interaction of the Galilean satellites with the Jovian
- 815 magnetosphere (Vol. 103). <u>http://doi.org/10.1029/97JE03370</u>

816

- 817 Neubauer, F. M. (1990). Satellite plasma interactions. Advances in Space Research, 10, 25–
- 818 38. <u>http://doi.org/10.1016/0273-1177(90)90083-C</u>

819

- 820 Nykyri, K., & Otto, A. (2001). Plasma transport at the magnetospheric boundary due to
- 821 reconnection in Kelvin-Helmholtz vortices. Geophysical Research Letters, 28(18), 3565–
- 822 3568. <u>https://doi.org/10.1029/2001GL013239</u>

- 824 Owen, C., Taylor, M., Krauklis, I., Fazakerley, A., Dunlop, M., & Bosqued, J. (2004).
- 825 Cluster observations of surface waves on the dawn flank magnetopause. Annales
- 826 Geophysicae, 22(3). pp. 971-983. ISSN 09927689, 22. <u>http://doi.org/10.5194/angeo-22-971-</u>
- 827 <u>2004</u>

- 829 Paral, J., & Rankin, R. (2013). Dawn–dusk asymmetry in the Kelvin–Helmholtz instability at
- 830 Mercury. Nature Communications, 4 (1), 1645. <u>https://doi.org/10.1038/ncomms2676</u>

831

- Schubert, G., Zhang, K., Kivelson, M. G., & Anderson, J. D. (1996). The magnetic field and
 internal structure of Ganymede. Nature, 384 (6609), 544–545.
- 834 https://doi.org/10.1038/384544a0

835

- 836 Slavin, J., Acun^a, M., Anderson, B., Baker, D., Benna, M., Gloeckler, G., . . . Zurbuchen, T.
- 837 (2008). Mercury's magnetosphere after Messenger's first flyby. Science (New York, N.Y.),
- 838 321, 85–9. <u>http://doi.org/10.1126/science.1159040</u>
- 839
- 840 Southwood, D. J. (1968). The hydromagnetic stability of the magnetospheric boundary.
- 841 Planetary and Space Science, 16, 587-605.

843	Southwood, D. J. (1979). Magnetopause kelvin-helmholtz instability. In Proceedings of
844	magnetospheric boundary layers conference. Noordwijk, the Netherlands.

- 846 Sundberg, T., Boardsen, S. A., Slavin, J. A., Anderson, B. J., Korth, H., Zurbuchen, T. H., ...
- 847 Solomon, S. C. (2012). Mercury orbital observations of large-amplitude Kelvin-Helmholtz
- 848 waves at Mercury's magnetopause. Journal of Geophysical Research: Space Physics,

849 117(A4). https://doi.org/10.1029/2011JA017268

850

- 851 Sundberg, T., Boardsen, S. A., Slavin, J. A., Blomberg, L. G., & Korth,
- H. (2010). The Kelvin–Helmholtz instability at Mercury: An assessment. Planetary and
- 853 Space Science, 58(11), 1434–1441. https://doi.org/10.1016/j.pss.2010.06.008

854

- Thomas, V. A., & Winske, D. (1993, 2020/06/18). Kinetic simulations of the Kelvin-
- 856 Helmholtz instability at the magnetopause. Journal of Geophysical Research: Space Physics,

857 98(A7), 11425–11438. https://doi.org/10.1029/93JA00604

858

- 859 Tóth, G., Jia, X., Markidis, S., Peng, I. B., Chen, Y., Daldorff, L. K. S., ... Dorelli, J. C.
- 860 (2016). Extended magnetohydrodynamics with embedded particle-in-cell simulation of
- 861 Ganymede's magnetosphere. Journal of Geophysical Research: Space Physics, 121(2), 1273–
- 862 1293. <u>https://doi.org/10.1002/2015JA021997</u>

- 864 Volwerk, M., Jia, X., Paranicas, C., Kurth, W. S., Kivelson, M. G., & Khurana, K. K. (2013).
- 865 Ulf waves in Ganymede's upstream magnetosphere. Annales Geophysicae, 31(1), 45–59.
- 866 <u>https://doi.org/10.5194/angeo-31-45-2013</u>

- 868 Volwerk, M., Kivelson, M. G., Khurana, K. K., & McPherron, R. L. (1999). Probing
- 869 Ganymede's magnetosphere with field line resonances. Journal of Geophysical Research:
- 870 Space Physics, 104(A7), 14729–14738. <u>https://doi.org/10.1029/1999JA900161</u>

871

- 872 Williams, D. J., Mauk, B., & McEntire, R. W. (1997). Trapped electrons in Ganymede's
- 873 magnetic field. Geophysical Research Letters, 24(23), 2953–2956.
- 874 <u>https://doi.org/10.1029/97GL03003</u>

- Williams, D. J., Mauk, B. H., McEntire, R. W., Roelof, E. C., Armstrong, T. P., Wilken, B., .
- 877 . . Murphy, N. (1997). Energetic particle signatures at Ganymede: Implications for
- 878 Ganymede's magnetic field. Geophysical Research Letters, 24(17), 2163–2166.
- 879 <u>https://doi.org/10.1029/97GL01931</u>
- 880
- Zhou, H., Tóth, G., Jia, X., & Chen, Y. (2020). Reconnection-driven dynamics at
- 882 Ganymede's upstream magnetosphere: 3d global hall MHD and MHD-EPIC simulations.
- Journal of Geophysical Research: Space Physics, n/a (n/a), e2020JA028162.
- 884 <u>https://doi.org/10.1029/2020JA028162</u>

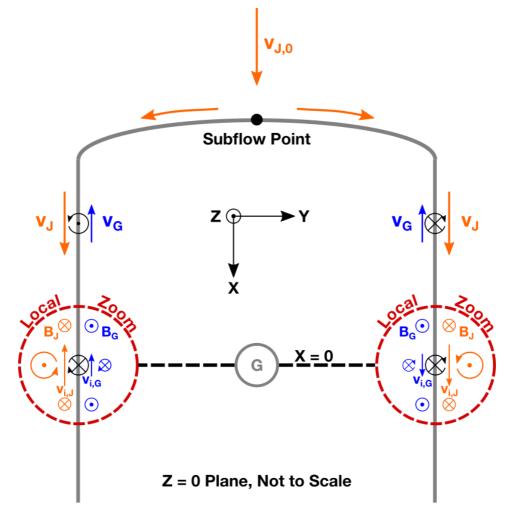
	Gyroradius (km) $R = \frac{M}{QB} \sqrt{\frac{E}{M}}$	Gyrofrequency (s ⁻¹) $\Omega = \frac{QB}{M}$	Gyro-viscous Coefficient (m ² /s) $v = \frac{R^2\Omega}{4}$
Jovian-side	62.91	0.46	4.51 × 10 ⁸
Ganymedean-side	4.75	0.73	-4.11×10^{6}

Note: Symbol meanings are as follow: M/Q = mass-to-charge ratio, B = magnetic fieldstrength, E = ion energy. All parameters are in SI units. The gyro-viscous coefficient is negative if the ion gyrates with southward vorticity.

$A_{i}\left(nT ight)$	γ (s ⁻¹)				
	0.01	0.1	1	10	
1	14.89	1.49	0.15	0.01	
5	9.68	0.97	0.10	<0.01	
10	7.44	0.74	0.07	<0.01	
15	6.13	0.61	0.06	<0.01	
20	5.20	0.52	0.05	<0.01	

890 Table 2: Distance Travelled by a K-H Wave before Forming a Nonlinear Vortex

891 Note: Distances are in R_G . The K-H vortex threshold is $A_f = 100$ nT and the K-H wave 892 propagation speed is $v_p = 85$ km/s. Bold and italicized distance numbers exceed 893 Ganymede's magnetotail length, set to be 9 R_G .



Far-Jupiter Flank

Near-Jupiter Flank

895 Figure 1: A schematic diagram of K-H instability growth on Ganymede's magnetopause flanks in the equatorial plane of the GphiO coordinate system. Bulk plasma velocities on 896 897 Jovian (v_J, orange arrows) and Ganymedean (v_G, blue arrows) produce vorticities (black circular arrows) in opposite directions between the two flanks. Local magnetic field 898 899 orientations (B_J, B_G) and plasma ion gyromotions (orange/blue circular arrows) are shown 900 inside zoom windows (red dashed lines) at (X = 0, Z = 0) flank points. Subsequent ion velocities on Jovian (v_{i,J}, orange arrows) and Ganymedean (v_{i,G}, blue arrows) produce ion 901 vorticities (black circular arrows) in the same direction on both flanks. The diagram is not to 902 903 scale.

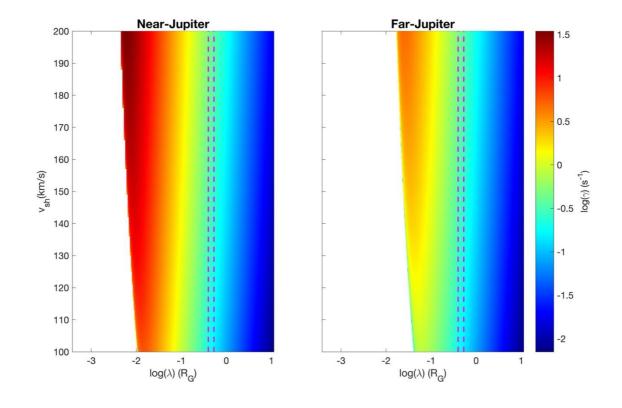


Figure 2: K-H instability growth rates at Ganymede's near-Jupiter and far-Jupiter equatorial magnetopause flank points, with respect to the logarithm of K-H wavelengths on the horizontal axis and the bulk flow shear on the vertical axis. Typical Ganymedean K-H wavelength ranges are enclosed by dashed magenta lines.

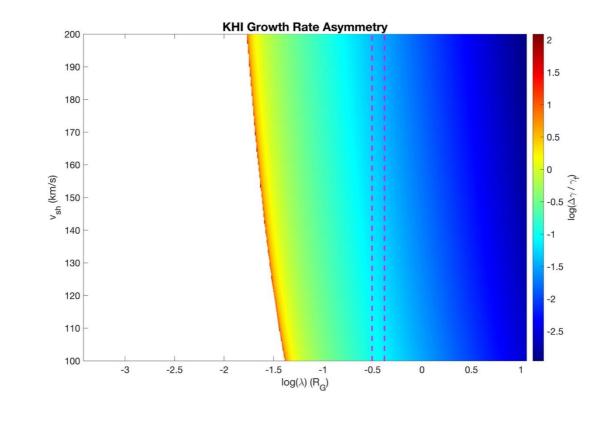


Figure 3: K-H instability growth rate asymmetry between Ganymede's near-Jupiter and farJupiter magnetopause flanks, expressed as a fraction of far-Jupiter growth rate value. The
format is the same as Figure 2.

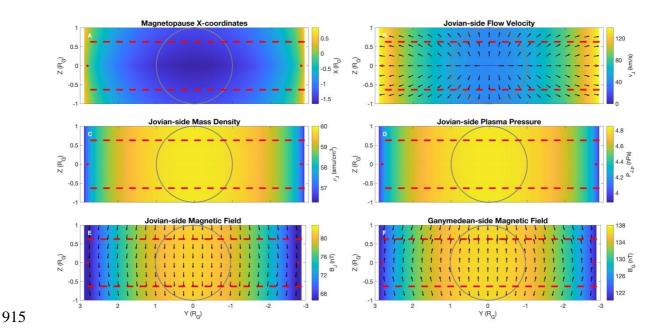
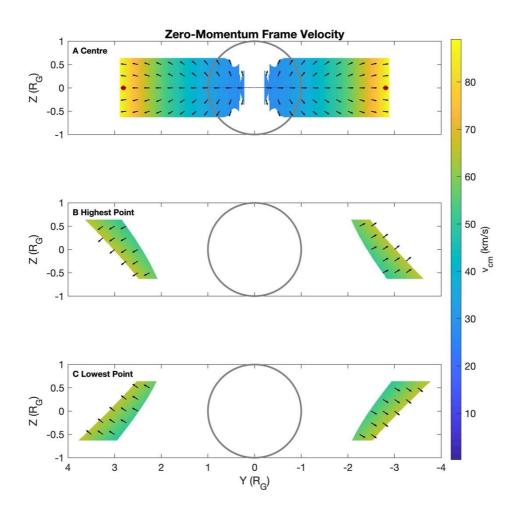


Figure 4: Near-magnetopause plasma and magnetic conditions computed by a steady-state analytical model of Ganymede's magnetopause (adapted from Kaweeyanun et al., 2020). Parameters shown are (a) magnetopause X-coordinates, (b) Jovian-side bulk flow velocity, (c) Jovian-side plasma mass density, (d) Jovian-side plasma pressure, (e) Jovian-side magnetic field, and (f) Ganymedean-side magnetic field. In each subplot, the closed-field region between two red dashed lines while the two red dots denote equatorial flank points where K-H instability growth rates are calculated in Section 2. Ganymede is outlined in grey



925 Figure 5: K-H instability onset assessment when Ganymede lies at (a) center of Jovian 926 plasma sheet and (b/c) highest/lowest points relative to the plasma sheet. K-H unstable 927 locations correspond to colored regions. The shared color bar denotes the speed, and the 928 normalized arrows denotes the direction, of zero-momentum frame velocity for the linear K-929 H wave. Red dots in Figure 5a show equatorial flank points and Ganymede is outlined in 930 grey.

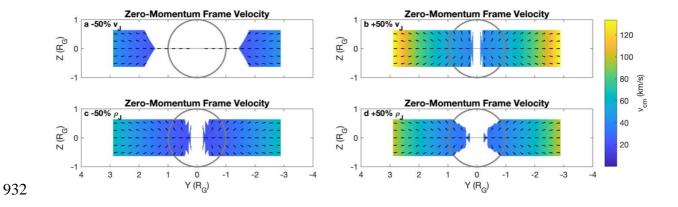
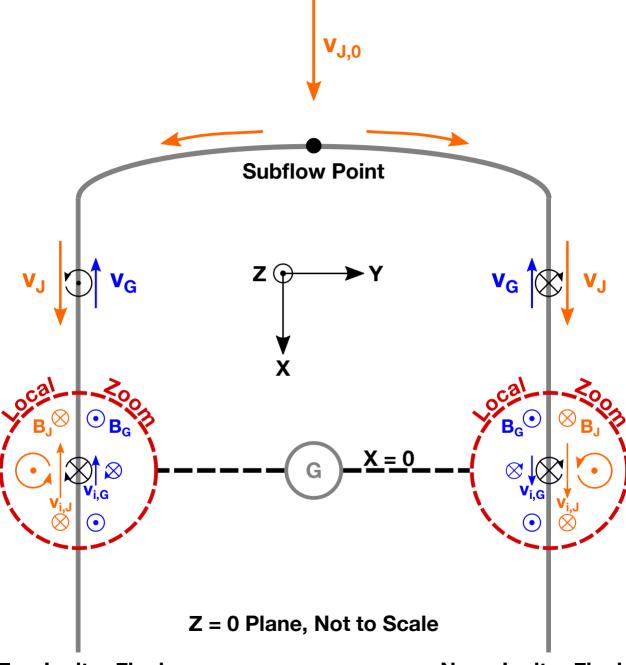


Figure 6: K-H instability onset assessment when Ganymede lies at center of the Jovian
plasma sheet, but with Jovian-side plasma conditions varied to simulate temporal effects.
Parameters considered are (a) -50% bulk flow speed, (b) +50% bulk flow speed, (c) -50%
mass density, and (d) +50% mass density. The format is the same as Figure 5.

	Gyroradius (km)	Gyrofrequency (s ⁻¹)	Gyro-viscous	
	MF	$\Omega = \frac{QB}{T}$	Coefficient (m ² /s)	
	$\mathbf{R} = \frac{\mathbf{M}}{\mathbf{QB}} \sqrt{\frac{\mathbf{E}}{\mathbf{M}}}$	$M = \frac{M}{M}$	$\nu = \frac{R^2\Omega}{4}$	
Jovian-side	62.91	0.46	4.51×10^{8}	
Ganymedean-side	4.75	0.73	-4.11×10^{6}	

$A_{i}\left(nT ight)$	γ (s ⁻¹)					
	0.01	0.1	1	10		
1	14.89	1.49	0.15	0.01		
5	9.68	0.97	0.10	<0.01		
10	7.44	0.74	0.07	<0.01		
15	6.13	0.61	0.06	<0.01		
20	5.20	0.52	0.05	<0.01		

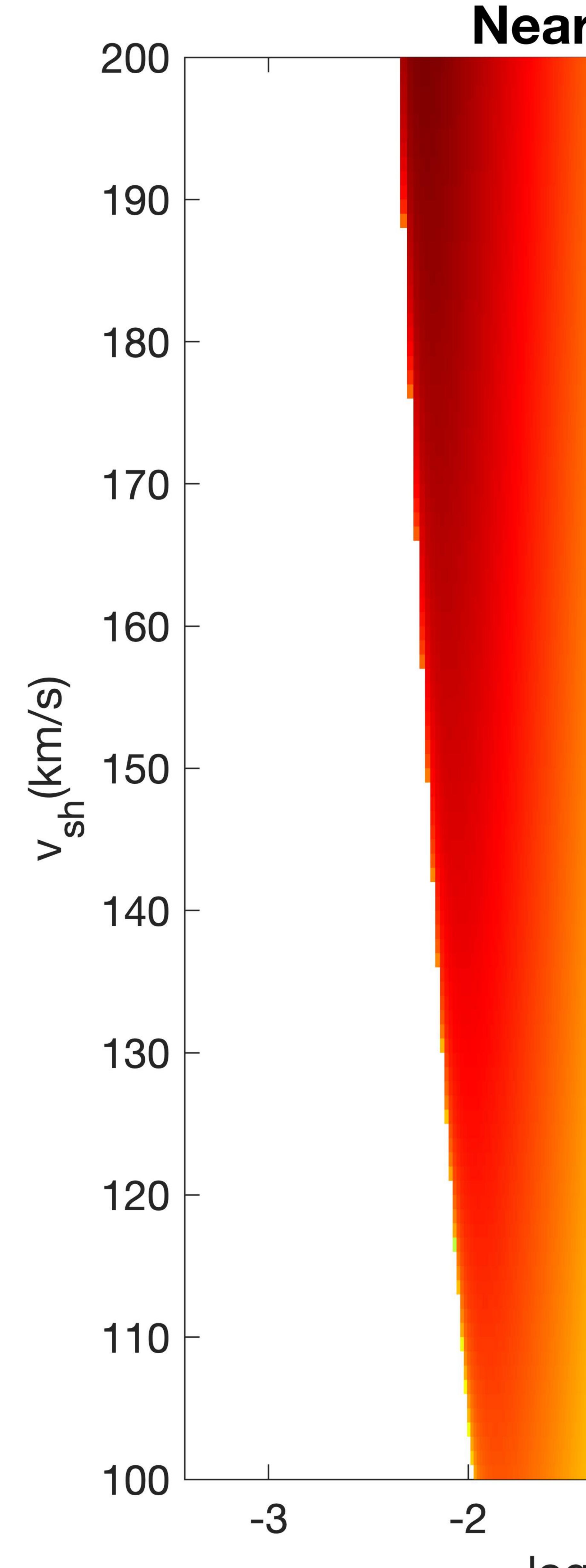
Figure 1.



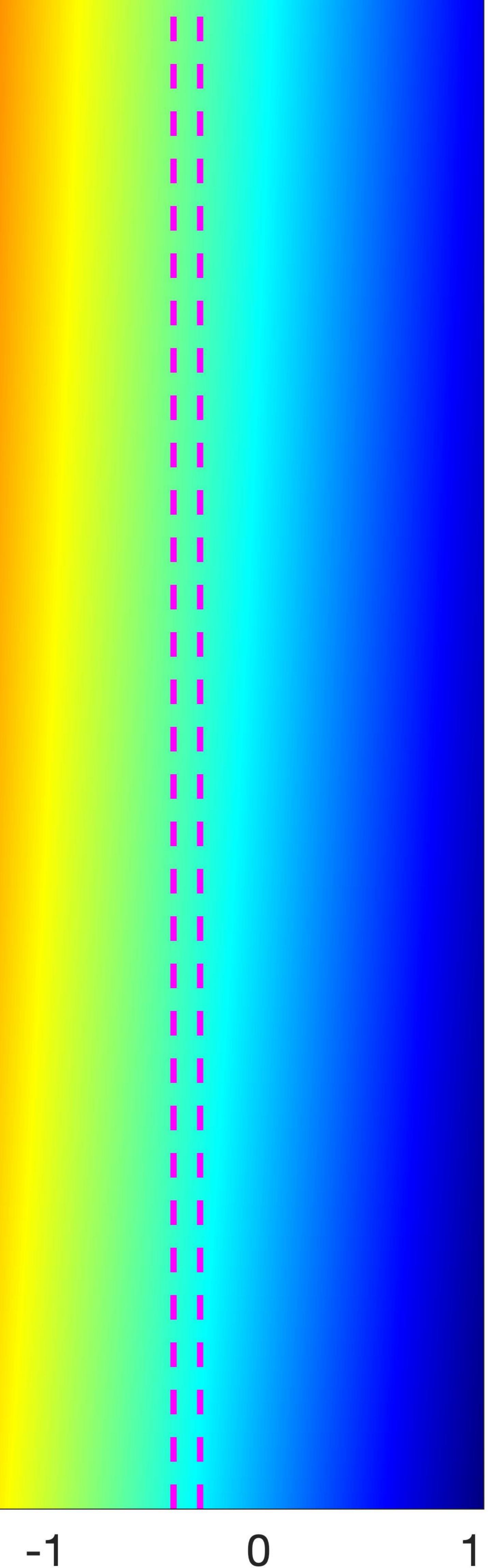
Far-Jupiter Flank

Near-Jupiter Flank

Figure 2.



Near-Jupiter



- $\log(\lambda) (R_G)$

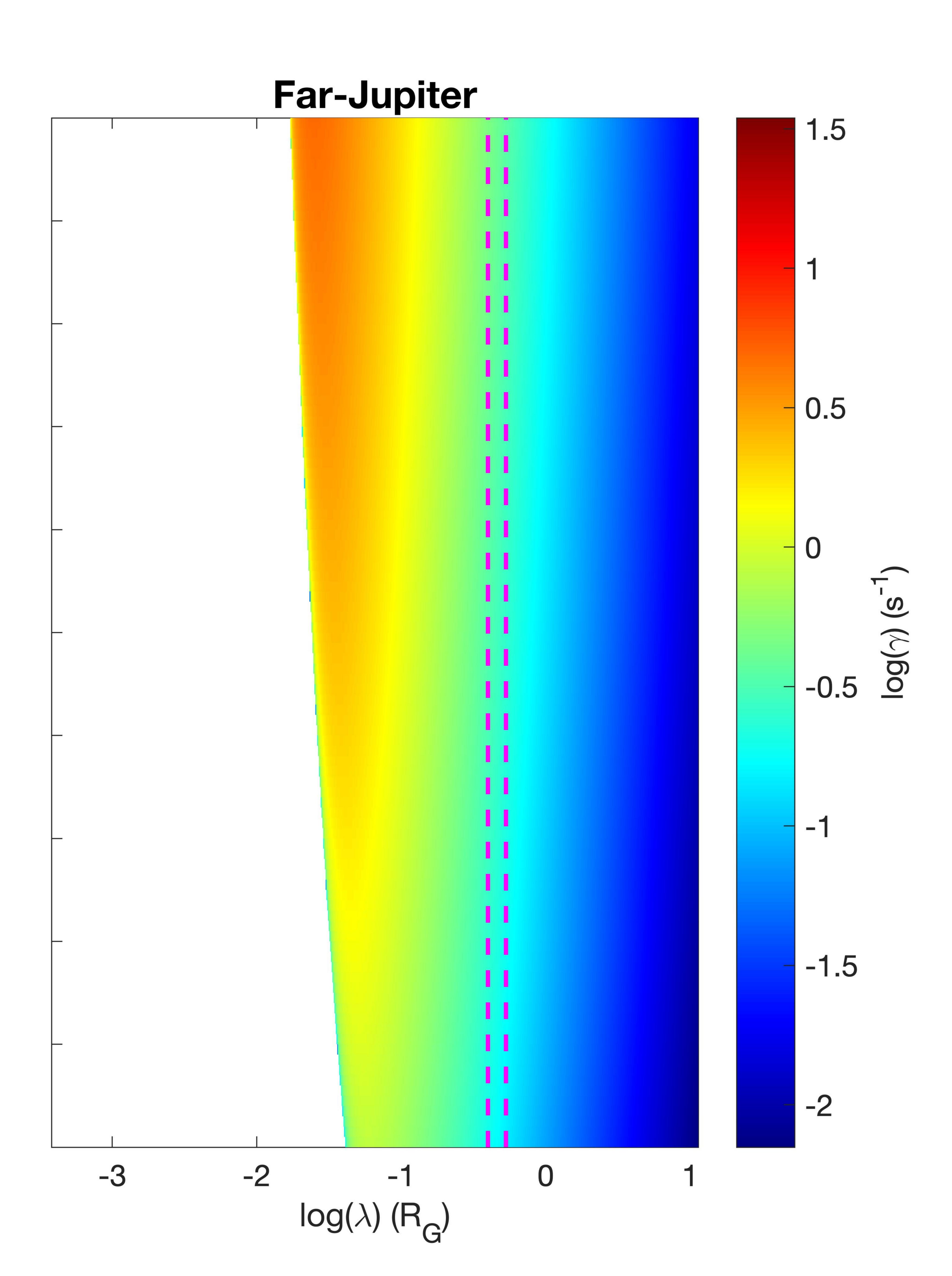
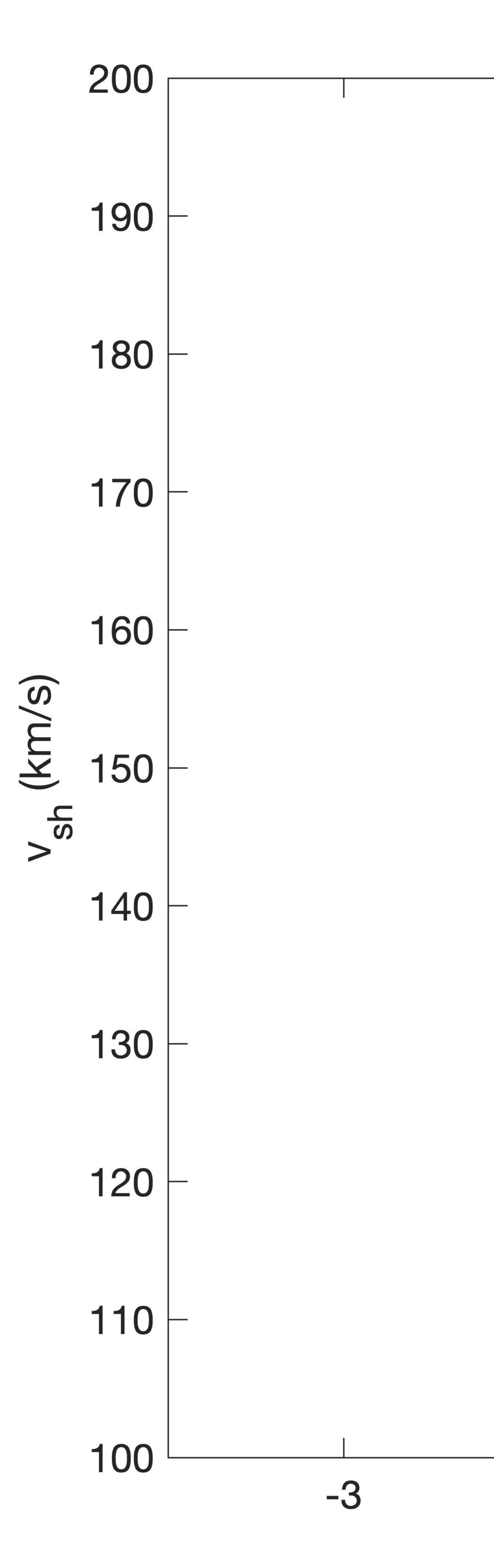


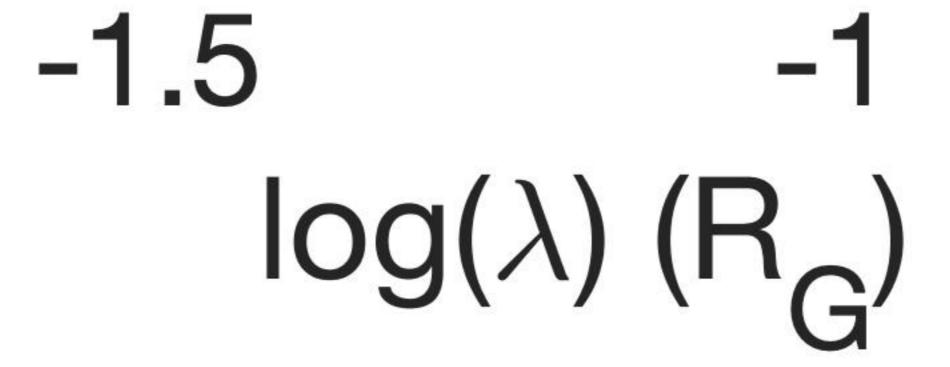
Figure 3.

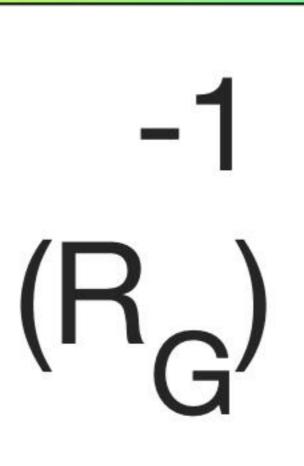


KHI Growth Rate Asymmetry



-2





-0.5

Т

1

Т

Т

L

н

н

L

Т

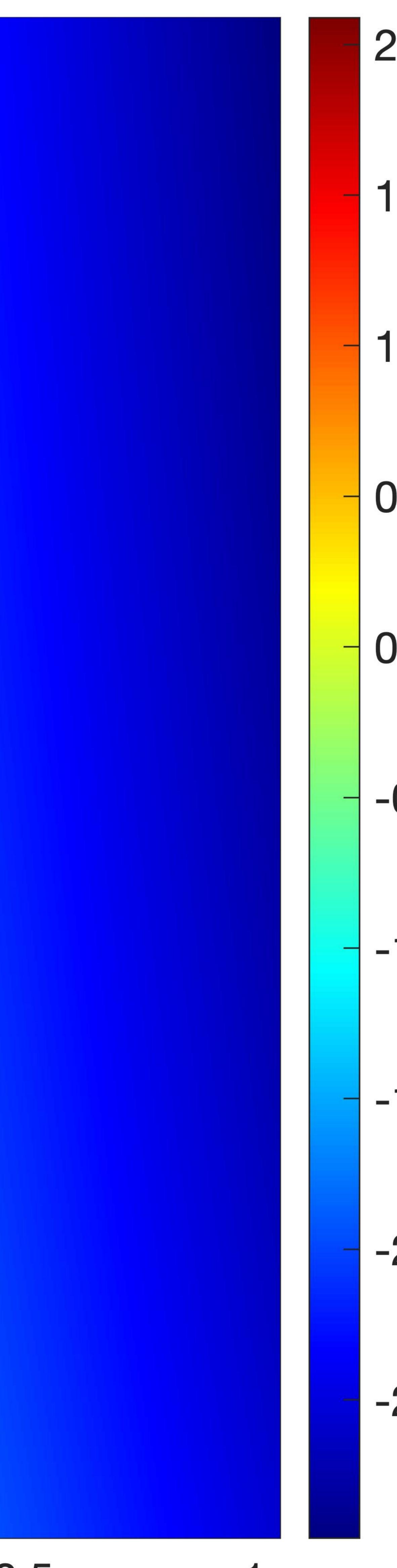
L

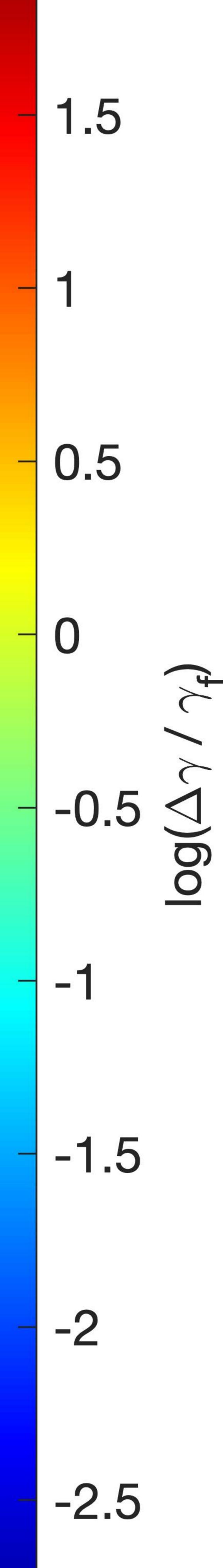
.

-

1

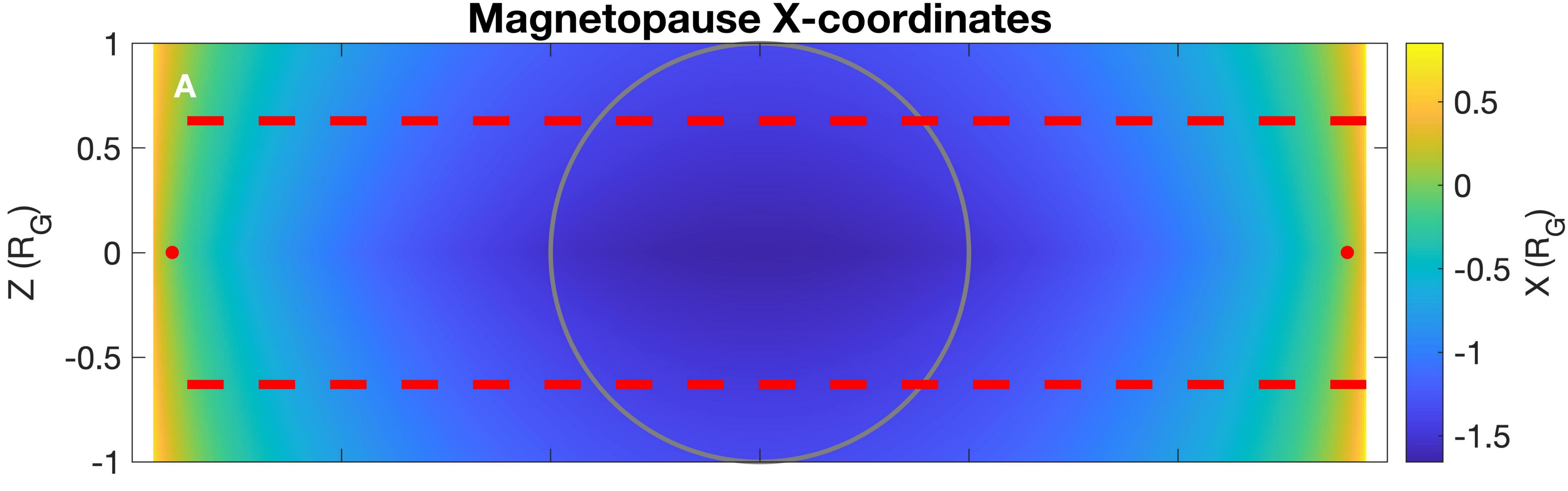
1

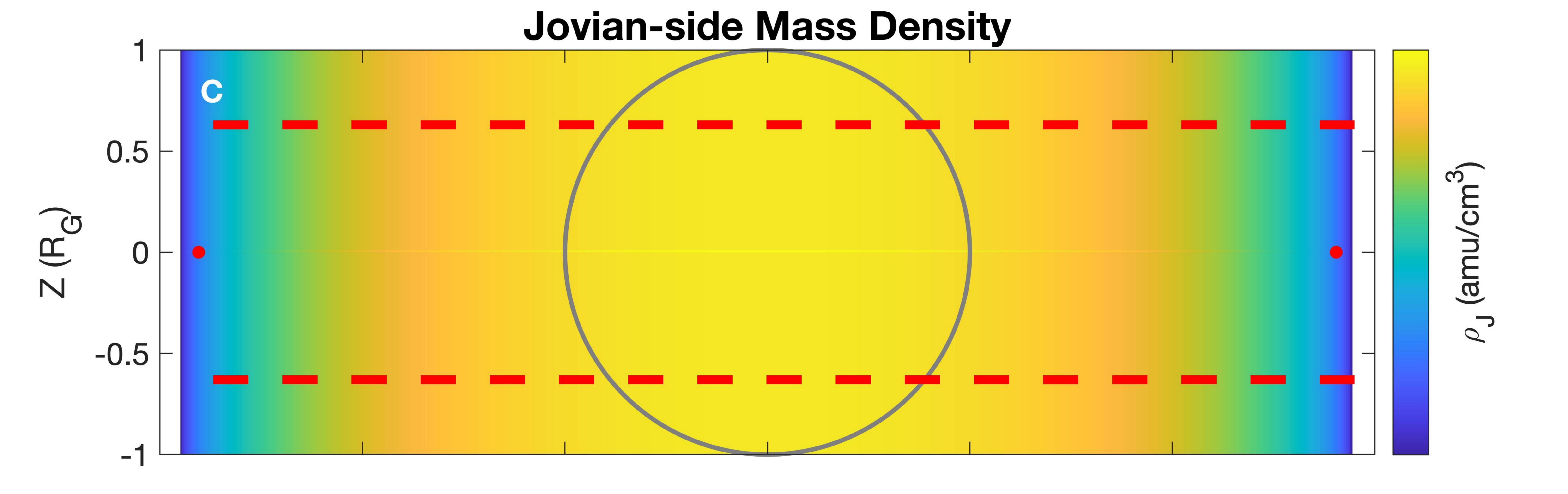


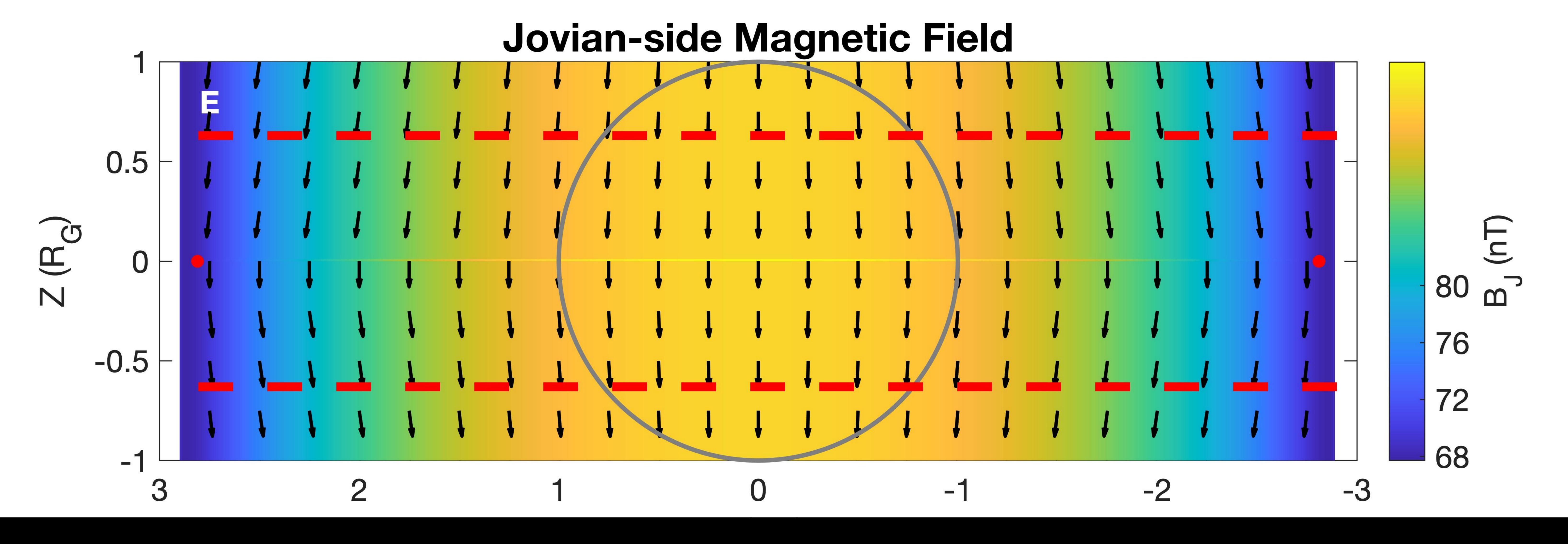


0.5

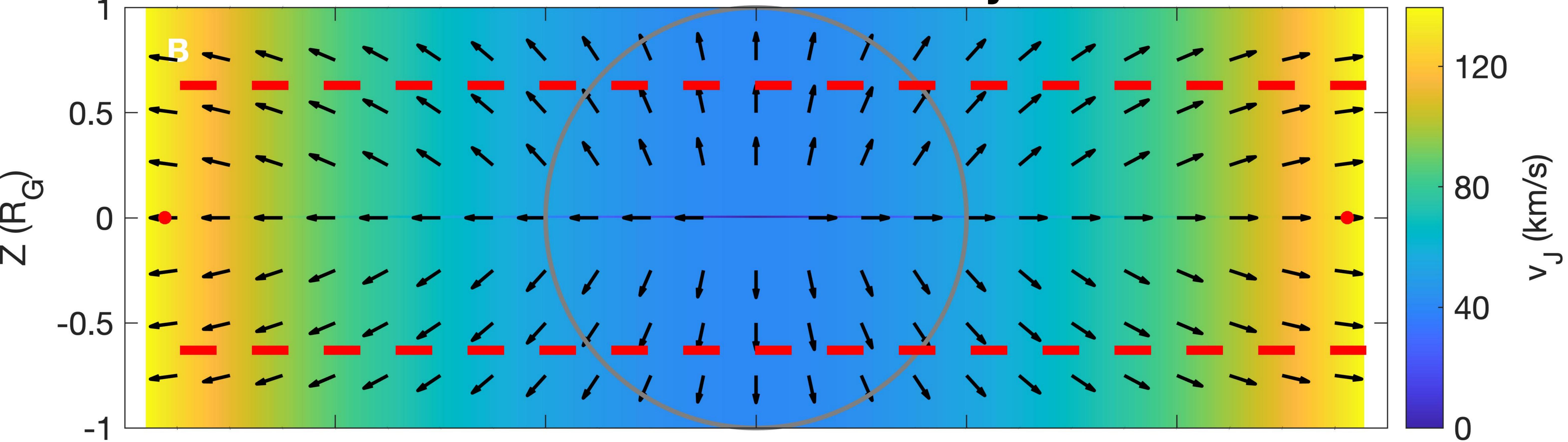
Figure 4.

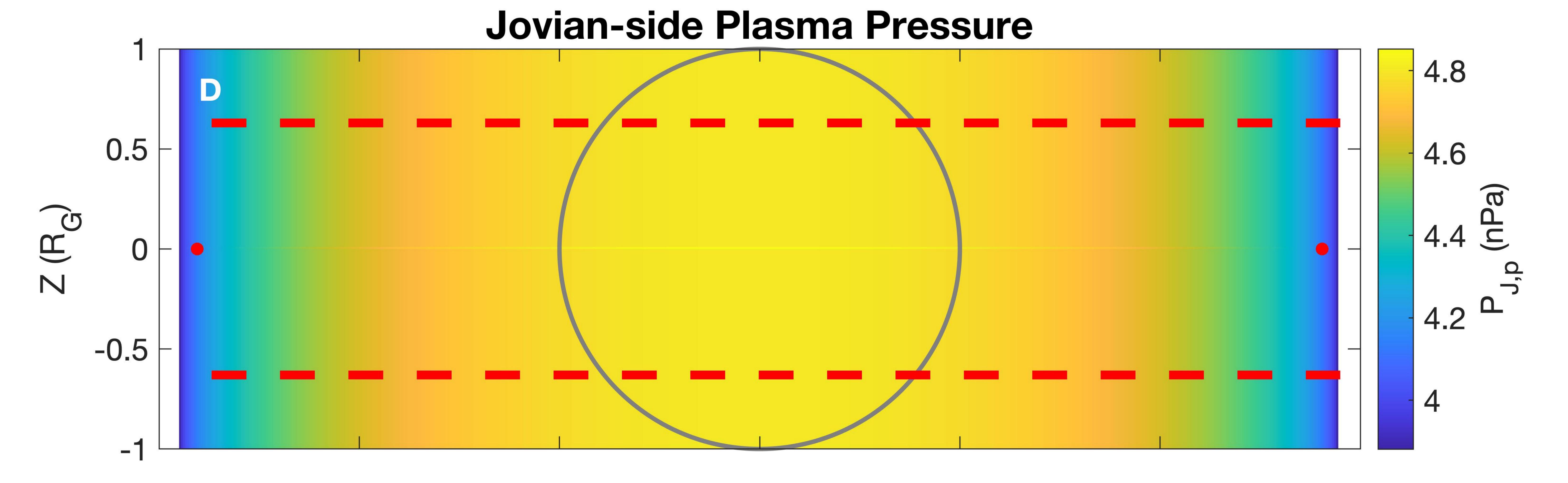












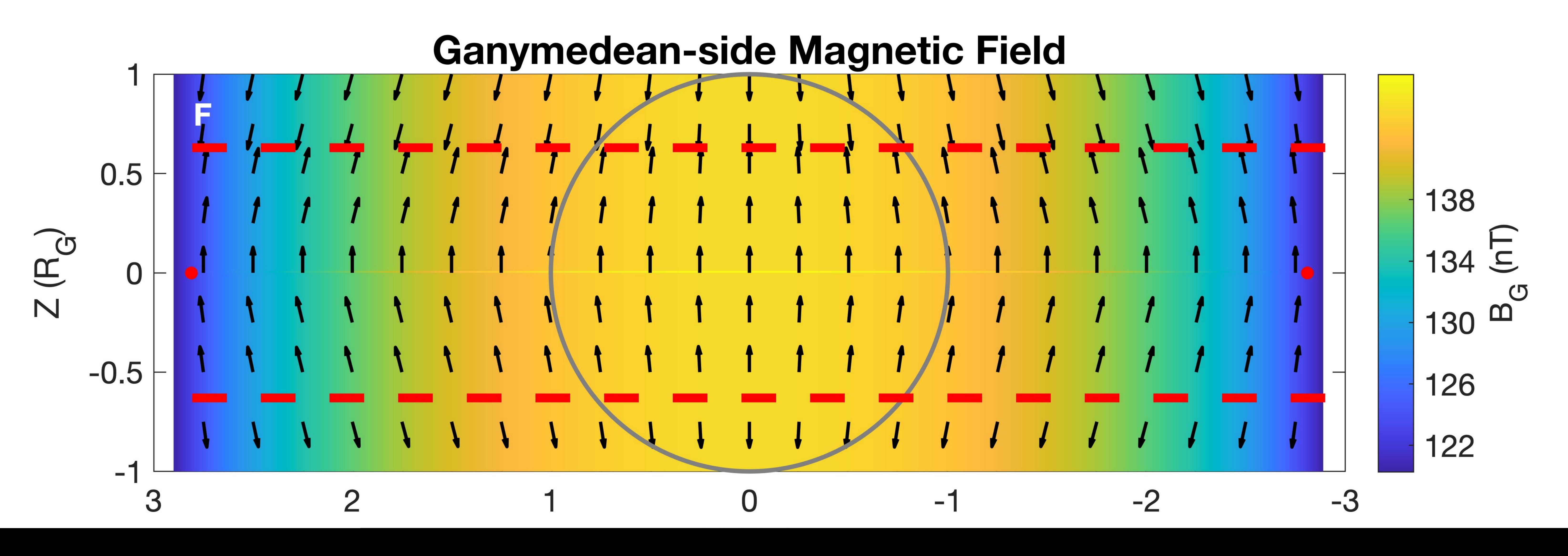


Figure 5.

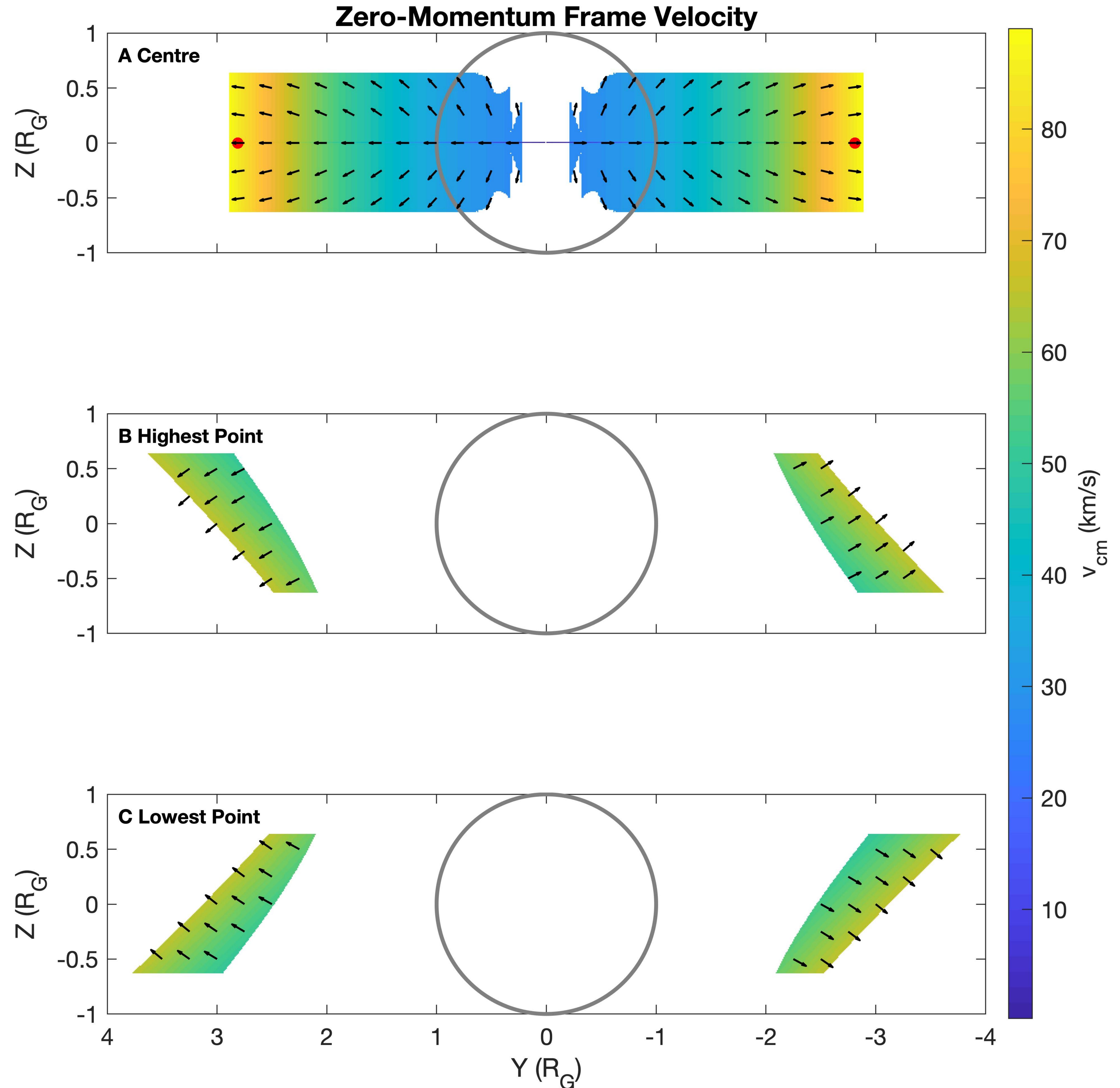
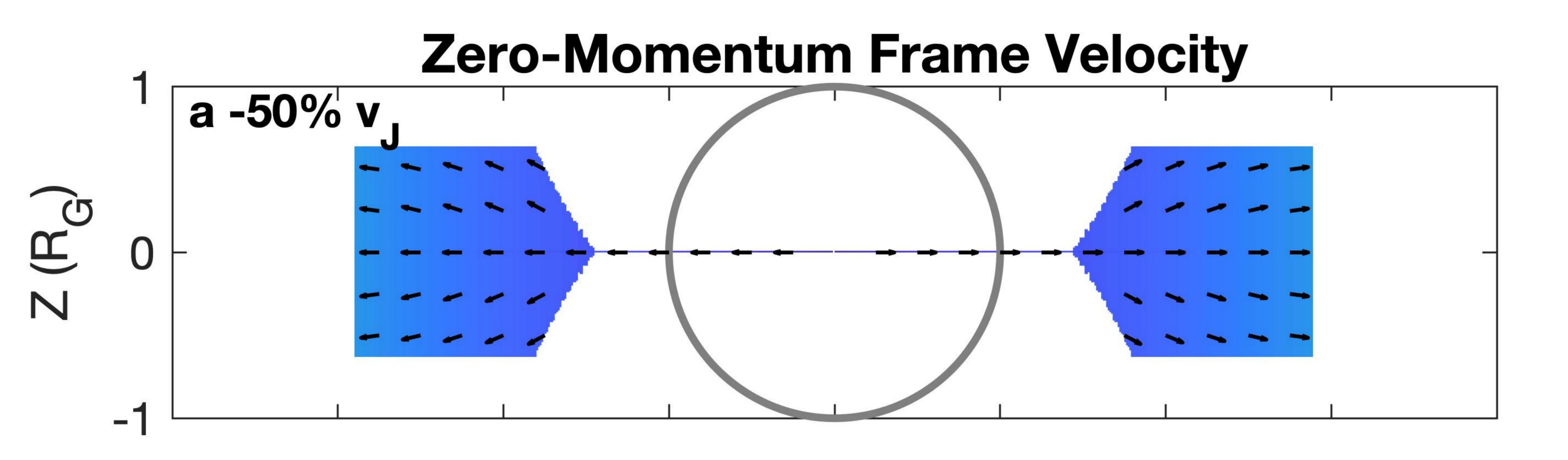
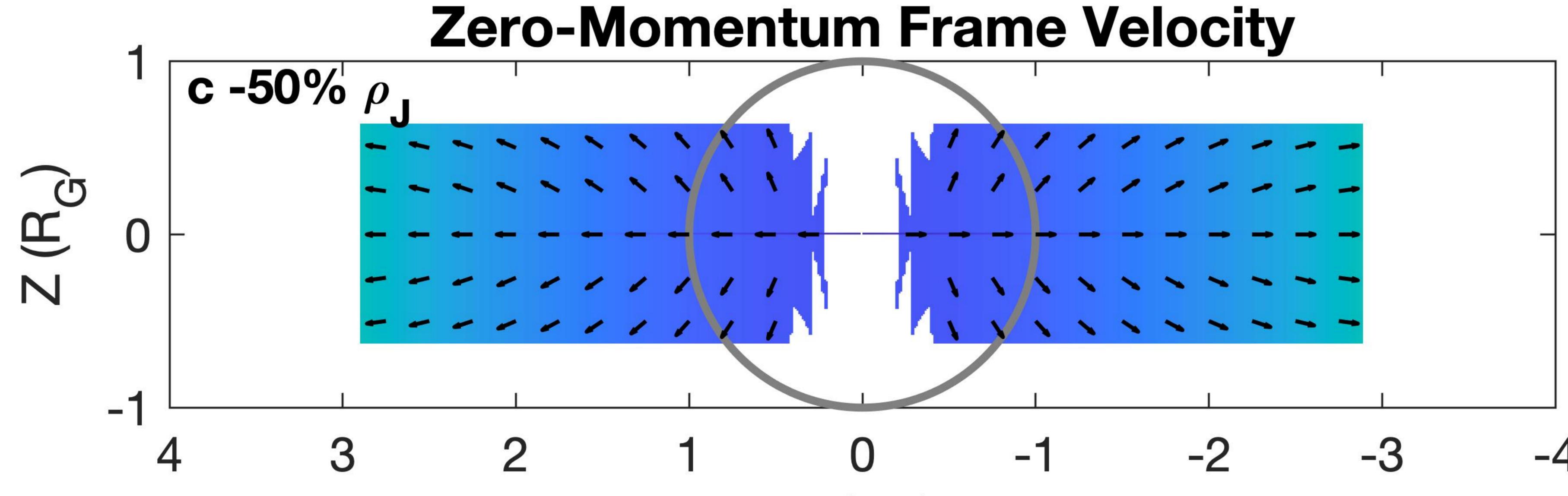


Figure 6.





V (R

Ц, N

L L

